Effect of Ni alloying on the microstructural evolution and mechanical properties of two duplex light-weight steels during different annealing temperatures: experiment and phase-field simulation

Alireza Rahnama[☆], Hiren Kotadia, Seetharaman Sridhar

International Digital Laboratory, Warwick Manufacturing Group, University of Warwick, Coventry, United Kingdom, CV4 7AL

Abstract

This paper presents a study of two lightweight steels, Fe-15Mn-10Al-0.8C-5Ni and Fe-15Mn-10Al-0.8C where strength is dependent upon the microstructure of 2nd phase precipitates. We investigate the effects of annealing temperature from 500 °C to 1050 °C on the precipitation of ordered phases size and morphology through phase-field modelling and experimental studies based on laboratory scale annealing and characterization. The chemical composition of carbides and B2 compounds as a function of isothermal annealing temperature and the matrix within which they formed are elucidated in this study. It is found that nano-sized disk-shaped B2 particles form at higher annealing temperatures (e.g. 900 °C and 1050 °C). The simulation results on carbides demonstrated the effects of energetic competition between interfacial energy and elastic strain energy on the morphological evolution of carbides. In addition to that, different ordering behaviours observed depending on the Ni content into the steel. The results demonstrate processing route designed through the phase-field simulations led to a better combination of strength and ductility. The tensile testing results indicate an increase in the strength and elongation when B2 precipitate morphology changes from micro-size faceted shape to nano-size disk-like particles.

Keywords: Low density steel, phase-field, intermetallic, κ-carbide, characterization

[☆]

[☆]Correspondong author: Alireza Rahnama, E-mail: a.rahnama@warwick.ac.uk

2010 MSC: 00-01, 99-00

1. Introduction

Lightweight steel alloys based on the Fe-Al-X alloying system (where X stands for Mn, Ni and/or C) combine the low density and corrosion resistance of aluminium with the low cost of manufacturability of steel based alloys. Fe-Mn-Al-C steels show significantly varying characteristics, depending on their respective Al concentration [1]. Depending on the constituent phases in their microstructure, lightweight steels can possess a wide range mechanical properties, with yield strength (YS) from 500 to 940 MPa, ultimate tensile strength (UTS) from 710 to 1020 MPa and tensile elongation (TE) from 8 to 78 % [1]. The key to obtain desired properties is dependent upon the ability to form complex strengthening precipitates [2, 3, 4, 5, 6, 7, 8, 9, 10]. In addition to κ-carbide, B2 (space group: Pm3M) and DO_3 (space group: Fm3M) ordered phases can also appear in the lightweight steels [17, 18]. Depending on the chemical composition and heat treatment conditions, β-Mn phases can also form in the microstructure of low density steels [11, 12, 13, 14, 15, 16]. In recent years, two main lightweight steel grades have been explored, namely ferritic Fe-Al (with an Al content up to 10 wt.% and additions of microalloying elements such as B, V, Ti and Nb ($<$0.03 wt.%)) and austenitic high-Mn (Fe-Al-Mn-C) steels [19, 20]. These steels possess a much better strength-to-weight ratio (specific strength) and toughness, and their density is reduced from $\sim$7.85 to 6.5 g/cm3 compared to transformation induced plasticity (TRIP) steels and twinning-induced plasticity (TWIP) steels [21, 22, 23, 24, 25, 26].

The formation and metallurgical control of the ferrite phase, $(Fe, Mn)_3AlC_x$ κ-carbide (perovskite-type crystal structure) and Al-containing intermetallic compounds, which determine the mechanical properties and may result in the poor rollability of this type of steel [26, 27, 28], is one the main aims of the current studies. The current challenges for manufacturing high Al lightweight steels include: re-oxidation and inclusion control of the liquid metal (increasing amount of Mn can lead to the formation of MnS inclusion, while decreasing Mn content results in the formation of α matrix with poor formability), clogging in continuous casting caused by the reactivity

2

of Al with the mold slag and cracking during cold working [29]. Lu and Qin showed

30   that cold workability of lightweight steels is affected by the lattice misfit and interface shape between κ and matrix [29]. They employed high density short duration electric current pulses for fabrication of this type of steel and demonstrate that electric current promotes the spheroidization and refinement of κ structure and leads to a decrease in the volume fraction of κ-carbides. Yao et al. also reported that the strain caused by the

35   κ/γ mismatch results in the occupation of Al sites in κ-phase by Mn atoms and thus leads to off-stoichiometric concentration of Al[30]. Other recent studies on duplex austenite-ferrite lightweight steels directed towards the effect of annealing temperature on the microstructural evolution and mechanical properties [31, 32], work hardening behaviour [33], and tensile deformation [34]. In 2014, the Minerals, Metals and

40   Materials Society organized a special lightweight steel meeting where recent research progress of low density steel was discussed and various in-depth studies on the metallurgical behaviours, thermodynamic calculations and hot deformation mechanisms of lightweight steels were published [35, 36, 37]. Ding et al. studied different grades of lightweight steels with Mn content less than 20% and Al content more than 8% (Fe-

45   12Mn-8Al-0.8C and Fe-18Mn-10Al-(0.8-1.2)C) and demonstrated that the ductility of duplex(austenite+ferrite) steels is less than that of steels with microstructure consisted of austenite and dispersed κ-carbide. However, their results showed that TRIPLEX lightweight steels (ferrite+austenite+κ-carbide) exhibits similar mechanical properties to that of austenitic lightweight steel [38, 39].

50   Nickel is one of the most effective alloying element for forming B2 with aluminium [40]. A recent study showed that nickel can expand the stability domain of B2 above the recrystallization temperature (800-900°C) of deformed austenite and improve the mechanical properties of lightweight steels [41]. However, although NiAl-type B2 intermetallics are inherently strong, their inadequate ductility at room temperature con-

55   stitutes a bottleneck that limits their widespread engineering applications [42]. One major reason for the low ductility of Ni-containing lightweight steels is the ordering of the α (body-centred cubic [BCC]) phase and its transformation to B2, which results in the formation of brittle, coarse ($> 100\mu$m, HV=492 HV$_{10}$) B2 stringer bands. One approach to improve the ductility is to form fine B2 precipitates in the α phase and,

3

60 thus, avoid the formation of coarse, brittle B2 stringer bands through an appropriate treatment [43]. In such a way, the α matrix provides the ductility whereas the nano-sized B2 precipitated in α yield the desirable strength. Therefore, this strategy can lead to an elevated strength and improved ductility. Moreover, the precipitation of coarse triangle-like ($> 2\mu$m) B2 precipitates at the grain boundaries results in very poor rolla-

65 bility making the industrial-scale production of this type of lightweight steels difficult. The κ-carbides and B2 particles contribute to the strength only if their shape, size and density are carefully designed [44] Otherwise, the precipitates will lead to brittleness, causing poor low-temperature ductility and the initiation of cracking (stress concentration) during thermomechanical processing.

70 The morphology of the precipitates can be explained in terms of the competing energetic contributions during the growth process [45]. Whereas the gradual increase in the importance of the strain energy relative to the interfacial energy may be known, the point during growth at which the effect is noticeable would naturally depend on the system, and the quantitative predictability of this point is critical when designing a micro-

75 structure in which the precipitate morphology is key. Also the additive Ni element substantially changes the precipitations of ordered phases and their chemical compositions. Such a study is of scientific importance since the precipitation behaviours of ordered phases are substantially different in austenite and ferrite due to the different formation processes as well as different coherencies with the matrix [42, 46, 47]. In

80 duplex microstructure, ferrite and austenite have different compositions. Thus, the composition of ordered phases will be different in each phase depending on the Ni content.

The first aim of the present study was to simulate the morphology of ordered phases in Fe-Mn-Al-C system for the evolution of κ-carbides and in Fe-Al and Fe-Al-Ni for

85 the evolution of B2 intermetallic compounds. This was done in order to better understand the microstructure evolution during the ordering processes at different isothermal holding temperatures in both γ and α phases. In this regard, phase-field modelling was employed because this method is currently considered as the most powerful approach for predicting the mesoscale morphological evolution [48, 49, 50, 51, 52, 53, 54, 55, 56,

90 57]. For the simulation of the B2 phase in binary Fe-Al and ternary Fe-Al-Ni systems,

4

a phase-field model was developed based on the Ginzburg-Landau theory initially proposed by Khachaturyan [58, 59] and further developed by Poduri and Chen [63]. In order to study the energetic contributions of interfacial energy and elastic strain energy on the morphological evolution of κ phase, a phase-field method connected to CALPHAD was employed based on our recent report [61], where a three sublattice model was used to allow intermixing between Mn and Fe atoms [62].

It is worth to mention that the primary purpose of these simulations was to investigate the combined effects of ordering and long-range elastic interaction on the growth and coarsening kinetics and the microstructural development of ordered phases in light weight steels. For this, composition order parameter was chosen since it enabled us to formulate the relationship between the gradient coefficients in the coarse grained free energy model and the interatomic interaction energies in the microscopic free energy model.

These simulations enabled us to design the thermal profile of heat treatments more precisely. Based on the simulation results, the heat treatments were then performed at $500°C, 700°C, 900°C$ and $1050°C$ for two grades of lightweight steels: the first grade contained 5%Ni and the second grade was Ni-free. For each heat treated sample, the following changes were investigated:

(i) The microstructural evolution e.g. the formation of ordered phases in the γ and α phases as a function of isothermal holding temperature.

(ii) The effect of Ni on the microstructural evolution in both disordered γ and α phases.

(iii) The change in the chemical compositions of the ordered phases as a function of temperature, the chemical composition of the bulk material and the phase within which they were formed.

(iv) The room temperature mechanical properties of each heat treated sample and its correlations with the constituent phases.

5

2. Methods

2.1. Experiments

2.1.1. Materials

Ni is expected to substantially change the precipitations of ordered phases and their chemical compositions and is one of the most effective alloying elements for forming B2 precipitates. A scientific study explaining the precipitation in austenite vs. ferrite and the role of Ni would be of technical importance when designing low density steels. For this purpose, two duplex alloys Fe-15Mn-10Al-0.8C-5Ni (S1) and Fe-15Mn-10Al-0.8C (S2) were selected for the current study. This enabled us to compare the effects of FeAl-type B2 intermetallic in austenite vs. ferrite (S1) and the role of Ni compounds on both the strength and ductility with those of NiAl-type B2 (S1 vs. S2). Furthermore, the base composition of Fe-15Mn-10Al-0.8C-5Ni was used as a base-line composition since it corresponds to the one reported in literature [41] where the role of ordered precipitates was noted but the kinetics of formation was not investigated and the formation of disk-like B2 particles was not reported.

The steels under study were produced by an induction melting furnace. The hot-rolled material was first solution-treated for 35 min at $1250°C$ in a protective argon atmosphere and then water quenched. The samples were prepared with dimensions of 3-mm (length), 3-mm (width) and 1-mm (thickness). Subsequent ordering treatments were applied at 500 °C and 700 °C (for κ and B2 ordering), and 900 °C for B2 ordering. We also performed an annealing treatment at 1050 °C because, based on our simulations, we anticipated that Ni-enriched nanosized B2 precipitates can form in the α phase at this temperature. The reason to select such a high annealing temperature was only to validate our simulation results and these materials are not designed to withstand such high temperature. After each heat treatment, the samples were water-quenched.

2.1.2. Characterisation and tensile test

The ordered phases were characterized by selected-area diffraction patterns (SADPs), bright-field (BF) images of transmission electron microscopy (TEM) JEOL 2000FX. Thin foils for TEM observation were prepared by twin-jet polishing in a mixture of

6

10% perchloric acid and 90% ethanol with an applied potential of 25 V. The steel specimens were, also, polished and etched in a 5% nital solution and the microstructures were observed by a Carl Zeiss Sigma Field Emission Scanning Electron Microscope
150 (FE-SEM) operated at 20 kV. The equipment was fitted with high speed X-ray energy dispersive spectroscopy (EDS). The subsequent tensile testing was performed on sub-sized specimens according to ASTM E8M in an Instron 5800R system at a strain rate of $10^{-3}/s$.

2.2. Phase-field models

155 #### 2.2.1. B2 intermetallic compound

A microscopic phase-field model was employed based on the Ginzburg-Landau theory [58]. In this approach, the atomic configuration and morphology were expressed by single-site occupation probability functions $P_A(\mathbf{r},t)$, $P_B(\mathbf{r},t)$, and $P_C(\mathbf{r},t)$, which correspond to the probabilities of finding an A, B, or C atom at any given lattice site $\mathbf{r}$
160 at a given time t. Since $P_A(\mathbf{r},t)+P_B(\mathbf{r},t)+P_C(\mathbf{r},t)=1.0$ for a ternary system, only two equations are independent at each lattice site. Assuming the independent variables are $P_A(\mathbf{r},t)$ and $P_B(\mathbf{r},t)$, their evolution can be expressed as:

$$\frac{dP_A(\mathbf{r},t)}{dt} = \frac{1}{k_BT}\sum_{\mathbf{r}'}[L_{AA}(\mathbf{r}-\mathbf{r}')\frac{\partial F}{\partial P_A(\mathbf{r}',t)} + L_{AB}(\mathbf{r}-\mathbf{r}')\frac{\partial F}{\partial P_B(\mathbf{r}',t)}]$$

$$\frac{dP_B(\mathbf{r},t)}{dt} = \frac{1}{k_BT}\sum_{\mathbf{r}'}[L_{BA}(\mathbf{r}-\mathbf{r}')\frac{\partial F}{\partial P_A(\mathbf{r}',t)} + L_{BB}(\mathbf{r}-\mathbf{r}')\frac{\partial F}{\partial P_B(\mathbf{r}',t)}] \quad (1)$$

where k_B is the Boltzmann constant, T is the temperature, $L_{\alpha\beta}(\mathbf{r}-\mathbf{r}')$ (α and β=A, B or C) is the kinetic coefficient proportional to the exchange probabilities of
165 elementary diffusion jumps from the lattice site $\mathbf{r}$ to $\mathbf{r}'$ per unit of time and F is the total free energy of the system and can be expressed as:

7

$$F = -\frac{1}{2} \sum_{\mathbf{r}} \sum_{\mathbf{r}'} [V_{AB}(\mathbf{r} - \mathbf{r}') P_A(\mathbf{r}) P_B(\mathbf{r}') + V_{BC}(\mathbf{r} - \mathbf{r}') P_B(\mathbf{r}) P_C(\mathbf{r}')$$

$$+ V_{AC}(\mathbf{r} - \mathbf{r}') P_A(\mathbf{r}) P_C(\mathbf{r}')] + k_B T \sum_{\mathbf{r}} [P_A(\mathbf{r}) ln(P_A(\mathbf{r})) + P_B(\mathbf{r}) ln(P_A(\mathbf{r}))$$

$$+ P_C(\mathbf{r}) ln(P_C(\mathbf{r}))] \quad (2)$$

$V_{AB}(\mathbf{r} - \mathbf{r}')$ is the effective interactive energies between A and B at lattice site $\mathbf{r}$ and $\mathbf{r}'$ which contains both the short-range chemical interaction and the long-range strain-induced elastic interaction. Hence, we can write:

$$V_{AB}(\mathbf{r} - \mathbf{r}') = V_{AB}(\mathbf{r} - \mathbf{r}')_{ch} + V_{AB}(\mathbf{r} - \mathbf{r}')_{el} \quad (3)$$

170   In the current study, the fourth nearest-neighbour interatomic model was used, and the data for the interchange energies were deducted from Refs [63, 64, 65]. Fourier transforming both side of the kinetic equation (1) gives:

$$\frac{d\tilde{P}_A(\mathbf{k},t)}{dt} = \frac{\tilde{L}_{AA}(\mathbf{k})}{k_B T} \{\tilde{V}_{AC}(\mathbf{k})\tilde{P}_A(\mathbf{k},t) + \frac{1}{2}[-\tilde{V}_{AB}(\mathbf{k}) + \tilde{V}_{BC}(\mathbf{k}) + \tilde{V}_{AC}(\mathbf{k})]\tilde{P}_B(\mathbf{k},t)$$

$$+ k_B T \{ln(\frac{P_A(\mathbf{r},t)}{1 - P_A(\mathbf{r},t) - P_B(\mathbf{r},t)})\}_k\} + \frac{\tilde{L}_{AB}(\mathbf{k})}{k_B T} \{\tilde{V}_{BC}(\mathbf{k})\tilde{P}_B(\mathbf{k},t)$$

$$+ \frac{1}{2}[-\tilde{V}_{AB}(\mathbf{k}) + \tilde{V}_{BC}(\mathbf{k}) + \tilde{V}_{AC}(\mathbf{k})]\tilde{P}_A(\mathbf{k},t) + k_B T \{ln(\frac{P_A(\mathbf{r},t)}{1 - P_A(\mathbf{r},t) - P_B(\mathbf{r},t)})\}_k\}$$

$$(4)$$

and

$$
\begin{aligned}
\frac{d\tilde{P}_B(\mathbf{k},t)}{dt} &= \frac{\tilde{L}_{BA}(\mathbf{k})}{k_B T}\{\tilde{V}_{AC}(\mathbf{k})\tilde{P}_A(\mathbf{k},t)+\frac{1}{2}[-\tilde{V}_{AB}(\mathbf{k})+\tilde{V}_{BC}(\mathbf{k})+\tilde{V}_{AC}(\mathbf{k})]\tilde{P}_B(\mathbf{k},t) \\
&\quad + k_B T\{ln(\frac{P_A(\mathbf{r},t)}{1-P_A(\mathbf{r},t)-P_B(\mathbf{r},t)})\}_k\} + \frac{\tilde{L}_{BB}(\mathbf{k})}{k_B T}\{\tilde{V}_{BC}(\mathbf{k})\tilde{P}_B(\mathbf{k},t) \\
&\quad +\frac{1}{2}[-\tilde{V}_{AB}(\mathbf{k})+\tilde{V}_{BC}(\mathbf{k})+\tilde{V}_{AC}(\mathbf{k})]\tilde{P}_A(\mathbf{k},t)+k_B T\{ln(\frac{P_B(\mathbf{r},t)}{1-P_A(\mathbf{r},t)-P_B(\mathbf{r},t)})\}_k\}
\end{aligned}
$$

$$(5)$$

where $\{ln(\frac{P_A(\mathbf{r},t)}{1-P_A(\mathbf{r},t)-P_B(\mathbf{r},t)})\}_k$, $\{ln(\frac{P_B(\mathbf{r},t)}{1-P_A(\mathbf{r},t)-P_B(\mathbf{r},t)})\}_k$, $\tilde{P}_A(\mathbf{k},t)$, $\tilde{P}_B(\mathbf{k},t)$, $\tilde{L}_{AA}(\mathbf{k})$, $\tilde{L}_{AB}(\mathbf{k})$, $\tilde{L}_{BA}(\mathbf{k})$, and $\tilde{L}_{BB}(\mathbf{k})$ are Fourier transforms of corresponding functions in real space.

2.2.2. κ-carbide

We simulated the precipitation of the ordered κ-carbide from both disordered γ and α phases, according to our recent report [61]. The Gibbs free energy for the multi-component Fe-Mn-Al-C systems was connected to the CALPHAD-type equations in order to provide realistic thermodynamic parametrization. We employed a Gibbs energy single formalism for the κ/γ and κ/α phases with a three-sublattice model for this quaternary system [62]. In these simulations, the order parameter of each element corresponds to long-range ordering in the κ phase because the order parameter is expressed using the element site fractions of a three-sublattice model in the CALPHAD method [61, 66].

The site fraction of each alloying element 'i' (i=Al, Mn, C or Va) on each sublattice 's' was represented by $y_i^{(s)}$. The molar Gibbs energy for the disordered γ and α and ordered κ-carbide phases was written as [61]:

9

$$G(c_i, y^{(s)i}) = G^{disord}(c_i) + \Delta G^{ord}$$

$$= [\sum_i c_i G_i^{disord} + RT \sum_i c_i ln c_i +$$

$$\sum_i \sum_{j>i} c_i c_j \sum_{n=0}^{m} ({}^n L_{i:j}^{disord}(c_i - c_j)^n) +$$

$$\sum_i \sum_{j>i} \sum_{k>j} c_i c_j c_k L_{i,j:k}^{disord}] + [\sum_i \sum_j \sum_k y_i^{(1)} y_j^{(2)} y_k^{(3)} \Delta G_{i:j:k}^{L'1_2} +$$

$$\frac{RT}{4} \sum_s \sum_i y_i^{(s)} ln(y_i^{(s)})$$

$$+ \sum_s \sum_i \sum_{j>i} y_i^{(s)} y_j^{(s)} \sum_{n=0}^{1} ({}^n L_{i:j}^{L'1_2}(y_i^{(s)} - y_j^{(s)}))] \quad (6)$$

c_i represents a mole fraction of element 'i', R refers to the gas constant, and T is temperature. G_i^{disord} represents a molar Gibbs energy of element 'i' with the structure of FCC or BCC. ${}^n L_{i,j}^{disord}$ and L_i^{disord}, j, k are binary and ternary interaction parameters, respectively. The total free energy F in the Fe-Mn-Al-C system included the local free energy density and the interface energy, was expressed as:

$$F \equiv \int_V (\frac{1}{V_m} G^{disord \ or \ L1_2} + \frac{\alpha}{2} \sum_{i=Mn,Al,(C,Va)}^{3} (\nabla c_i)^2$$

$$+ [\frac{\beta}{2} \sum_{i=Mn,Al,(C,Va)}^{3} (\nabla \phi_i^j)^2] + g_V^{el}) dV \quad (7)$$

where V_m refers to the molar volume which is assumed to be constant. α and β are the gradient energy coefficients for the compositions and order parameters, respectively. Interfacial anisotropy was introduced into the phase-field model by making β orientation-dependant [67]. G_V^{el} is the elastic energy density which was expressed as in Ref. [58]. The temporal evolution of the elemental concentrations and order parameters can be obtained by calculating the following non-linear Cahn-Hilliard diffusion

10

200 and time-dependant Ginzburg-Landau equations:

$$\frac{\partial c_i}{\partial t} = \sum_j \nabla.(\tilde{M}_{ij} \nabla \frac{\delta F}{\delta c_j}), \quad i = Mn, Al, (C, Va), \quad j = Mn, Al, (C, Va) \quad (8)$$

$$\frac{\partial \phi_i^j}{\partial t} = -L\frac{\delta F}{\delta \phi_i^j}, \quad i = Mn, Al, (C, Va), \quad j = 1, 2, 3 \quad (9)$$

where $\tilde{M}_{ij}$ and L are the diffusion mobility and the structural relaxation, respectively. The system size for the simulation is $300\Delta x \times 300\Delta x \times 300\Delta x$ (grid size: $\Delta x = 0.25nm$) for 3D single particle simulations. The thermodynamic parameters, elastic constants, coefficients and mobilities were taken from (Ref. [61, 62, 65, 67, 68,

205 69, 70]). The required values for the calculation of interfacial energies were determined by the methods and experimental values presented in a study by Doi [71], for instance: $0.152\,\mathrm{Jm}^{-2}$ for Fe-Al system with coherent interface, $0.74\,\mathrm{Jm}^{-2}$ for Fe-C system with incoherent interface, $0.014\,\mathrm{Jm}^{-2}$ for Ni-Al system with coherent interface. A semi-Implicit-Fourier-Spectral-Method [72] is used for numerical analysis with a periodical

210 boundary condition.

3. Results & discussion

3.1. Simulation results on B2

We performed four controlled phase-field simulations for four different annealing temperatures - $500^\circ C$, $700^\circ C$, $900^\circ C$, and $1050^\circ C$ - to determine whether there is any

215 difference in the B2 precipitation process in the α phase and to examine its compositional dependency on the formation temperature (Fig.1). We noted that two jumps in the composition order parameter (COP) occur when the simulations were performed at $900^\circ C$ and $1050^\circ C$ (Fig.1c and d). The first jump corresponds to the ordering process of the α phase and its transformation to B2 stringer bands. The second jump

220 corresponds to the precipitation of disk-like B2 particles in the ordered α phase. This finding is notably different from that of an earlier study [41] and motivated its experimental validation in the current study.
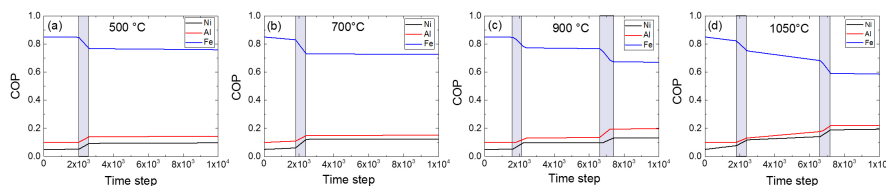
11

Figure 1: Variation of the COP with ageing time. (a) and (b) represent the changes in the COP for isothermal annealing at $500°C$ and $700°C$, respectively. After a jump at $t^* = 1800\Delta t$, a slight increase in the value of COP is evident. Phase-field simulation revealed that the Ni content is richer in the B2 particles formed at $700°C$. (c) and (d) represent the variations of the COP with ageing time for ordering treatments at $900°C$ and $1050°C$, respectively. Two jumps in the values occur: the first jump ($t^* = 1800\Delta t$) corresponds to the ordering of α at the start of the precipitation, and the second jump ($t^* = 6800\Delta t$) is related to the formation of disk-like B2 particles in the ordered BCC phase. Phase-field simulations revealed that the Ni content of the disk-like particles formed at $1050°C$ is richer than that of B2 compounds formed after annealing at $900°C$.

The variations of the COP for the binary Fe-Al system (Fig.2a) and the ternary Fe-Al-Ni system (Fig.2b) were computed. For the ternary Fe-Al-Ni system, Fe atoms were

²²⁵ substituted by Ni and Al atoms, forming NiAl-type B2 compounds. For the binary Fe-Al system, Fe atoms were replaced by Al, indicating the formation of FeAl-type B2. According to these figures, the compositional changes in all three elements occurred during the early stages of simulation in the presence of Ni (Fig.2b), whereas these changes occurred later in the absence of Ni (Fig.2a). Our simulation results for B2

²³⁰ intermetallic compounds revealed that the morphology of B2 depends on the matrix within which they precipitate: a disk-like shape in the α matrix (Fig.2 c) and a faceted interface with sharp edges in the γ phase (Fig.5d). The change in the morphology of the B2 particles is the direct manifestation of the orientation relationship with the matrix: B2 has a Kurdjumov-Sach (KS) relationship with the FCC γ phase and a cube-to-cube

²³⁵ relationship with the BCC α phase [73]. This morphology is technically important because the spheroidization of particles facilitates increasing their ductility while retaining desirable strength [43]. The formation of disk-like B2 particles in the α matrix means that the hard B2 stringer bands would no longer exist after heat treatments at higher temperature and instead the microstructure would consist of soft α phase which

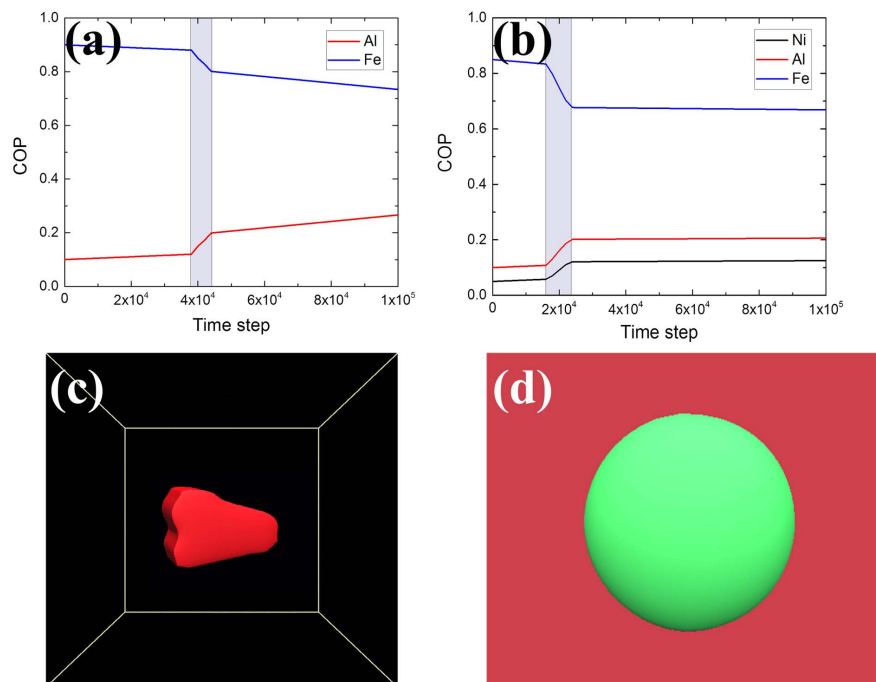²⁴⁰ provide the ductility and hard nanosized disk-like B2 particles as the strengthening secondary phase.

Figure 2: (a) Variation of the COP in the Fe-Al system with ageing time $t^* = 10000\Delta t$. (b) Variation of the COP in the Fe-Al-Ni system with ageing time $t^* = 10000\Delta t$. (c) Simulated morphology of a FeAl-type B2 particle in the γ phase $t^* = 10000\Delta t$. (d) Phase-field simulation of a NiAl-type B2 precipitate in the α matrix $t^* = 10000\Delta t$.

3.2. Simulation results on κ-carbide

We developed a phase-field method coupled with a Computer Coupling of Phase Diagrams and Thermochemistry (CALPHAD)-type database for three different scenar-
250 ios: interfacial energy as the only contributing energy with elastic strain ignored, elastic strain energy as the only contributing energy with interfacial energy of $10\ mJm^{-2}$, and finally, the contributions of both energies to the final morphology (Fig.3). To investigate each energetic contribution to the precipitation of a κ particle in the α phase, the total elastic strain energy E_{el} and total interfacial energy E_{int} within the simulation re-
250 gion were computed (Fig.3c). In addition, the change in the length of the κ precipitates along the [100], [010] and [001] directions was computed during the phase-field simulations (Fig.3d). Considering the interfacial energy only, the $L_{[100]}/L_{[010]}$ aspect ratio slightly increased (Fig.3d), whereas in the scenario where only the elastic strain energy

13

contributes, the $L_{[100]}/L_{[010]}$ aspect ratio continuously increased with a rate faster than

255   that of the scenario where only interfacial energy was considered as the contributing energy. The elongated needle-like κ-carbides in the α phase result from a high lattice mismatch between α and κ. Due to the high misfit value, the morphological evolution of the precipitates in the α phase was mainly determined by the elastic coherency term rather than by the interfacial energy contribution.

260   As shown in Fig.3a and b, κ-carbides contain two main morphologies: a faceted cuboidal shape in the γ-phase, and an elongated needle-like morphology in α. These results were in agreement with those determined experimentally [24, 46, 47]. Additionally, phase-field simulations demonstrated the interaction between the energetic contributions and the relative values of the interfacial energy and elastic strain energy.

265   The main difference between these two contributing energies was that elastic energy exists throughout the precipitate, whereas the interfacial energy only contributes to the γ/κ or α/κ interfaces. Expectedly, the total interfacial energy of the system was larger than the total elastic strain energy when the initial nucleus was small because, in the context, the area-to-volume ratio is high. As the κ precipitate grew, the value of the

270   area-to-volume ratio reduced, and the elastic energy contribution to the morphological evolution became dominant. Therefore, the interfacial energy determined the morphology of κ-carbides in the initial stages of the simulation, whereas the effect of the elastic strain energy became dominant as the precipitate grew.

Based on our simulation results, we performed the following experiments to inves-

275   tigate:

(i) the morphologies of ordered phases in both disordered γ and α phases,

(ii) the formation of disk-like B2 particles in α for heat treatments at $900°C$ and $1050°C$,

(iii) the variation of chemical compositions of ordered phases as a function of anneal-

280   ing temperature and the matrix within which they form and

(iv) the change in the room temperature mechanical properties as a function of annealing temperature and of the shape of ordered phases that were formed.
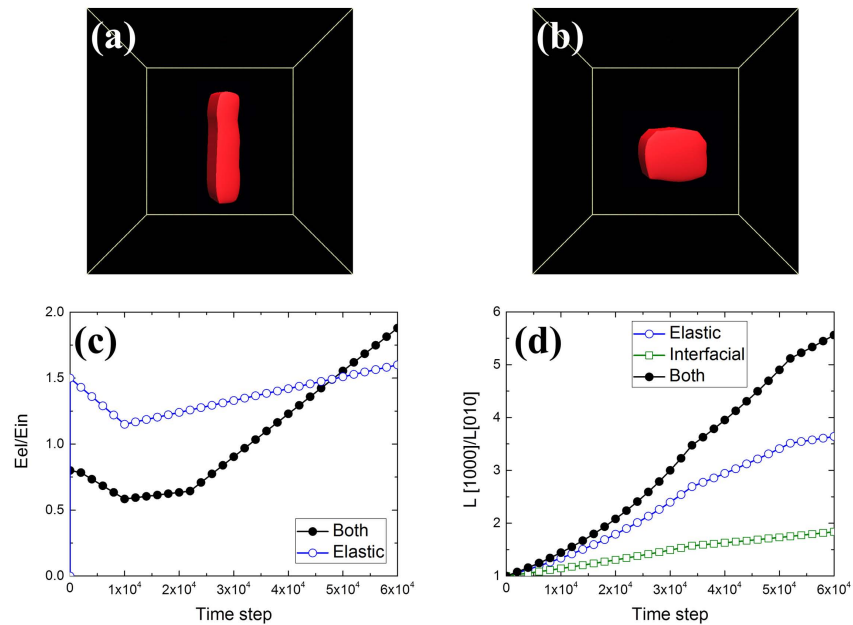
14

Figure 3: (a) The simulated morphology of κ-carbide ($t^* = 70000\Delta t$) in the α matrix. (b) The simulated morphology of a κ particle ($t^* = 70000\Delta t$) in the γ phase. (c) Evolution of the ratio of total elastic strain energy to total interfacial energy under different anisotropy conditions. (d) Evolution of the $l_{[100]}/l_{[010]}$ aspect ratio of κ precipitate in the α phase under different anisotropy conditions.

3.3. Microstructure before heat treatment

Fig.4a and b show the as-quenched microstructures of the S1 and S2 samples, re-

285 spectively. The microstructures of both samples consist of coarse-grain austenite (γ) and ferrite (α). The microstructures were examined under TEM and neither κ-phase nor B2 particles were observed in the as-quenched samples.
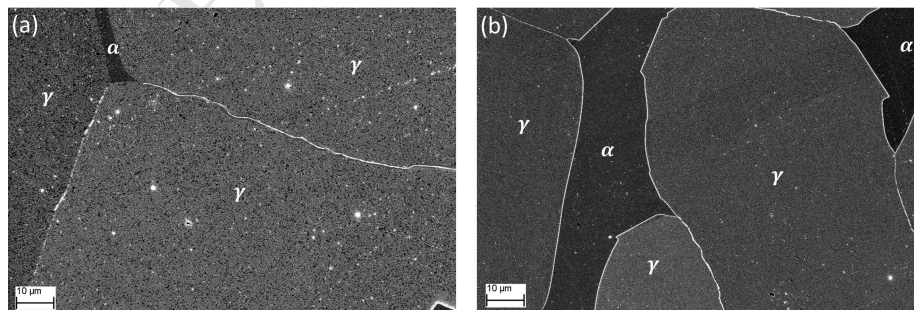

Figure 4: SEM micrographs of a) as quenched Fe-15Mn-10Al-0.8C-5Ni and b) as-quenched Fe-15Mn-10Al-0.8C.

3.4. Heat treatment at 500 °C

Fig.5 shows the SEM micrographs of S1 (Fig.5a) and S2 (Fig.5b) after isothermal
290 holding at $500°C$. The final microstructure of S1 is composed of $\gamma+\kappa$ and coarse NiAl-
type B2 intermetallics dispersed within the γ phase. The ferrite phase was transformed
to B2 by the ordering of the phase and the enrichment of Ni forming stringer-type
B2 (Fig.6). Coarse B2 intermetallic particles were formed both at grain boundaries and
within the γ phase. The microstructure of S2 after isothermal holding at $500°C$ consists
295 of γ, ferritic matrix (α) and the lamellar structure formed along the grain boundaries.
In the lamellar structure, there are fine ferrite and κ-carbide. Hence, the γ phase was
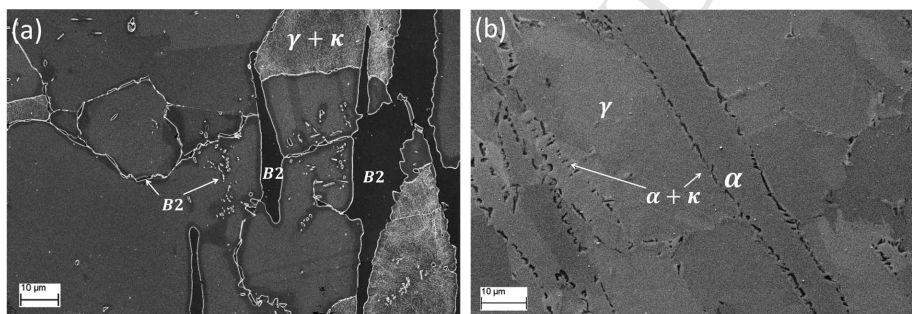partially decomposed into ferrite and needle-like κ-carbide.

Figure 5: SEM micrographs of (a) Fe-15Mn-10Al-0.8C-5Ni and (b) Fe-15Mn-10Al-0.8C after isothermal
holding at $500°C$.
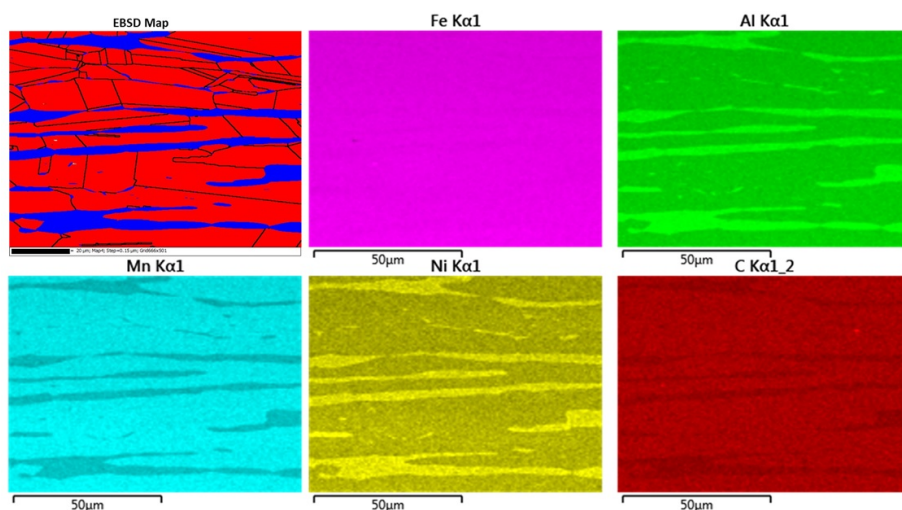
16

Figure 6: EBSD map (austenite is red and ferrite is blue) and corresponding elemental maps of Fe-15Mn-10Al-0.8C-5Ni after annealing at $500^\circ C$. This figure shows the partitioning of Ni (yellow) and Al (green) atoms into the α phase and hence the formation of NiAl-type B2 stringer bands.

Fig.7a,b,c and d show the TEM-BF micrographs of the steels after isothermal holding at $500^\circ C$ and corresponding SADPs. Fig.7a shows the TEM micrograph of S1

300 confirming that κ-phase was formed in the γ phase with size of less than 100 nm. No κ-carbide were found in the α phase due to the transformation of originally α phase to the thermodynamically stable B2-phase (Fig.7b). This is because Ni is a very strong intermetallic former with Al [41] and this type of intermetallics is generally thermodynamically more stable than κ-phase. [42, 74, 75]. In the absence of Ni (S2), the

305 needle-like κ-phase was observed in α (Fig.7c), while dense cuboid κ-carbide was detected in the γ phase (Fig.7d). In general, κ formed in the γ phase in the absence of Ni (S2) was smaller (less than 90 nm) and denser than that formed in the γ phase in the presence of Ni (S1).
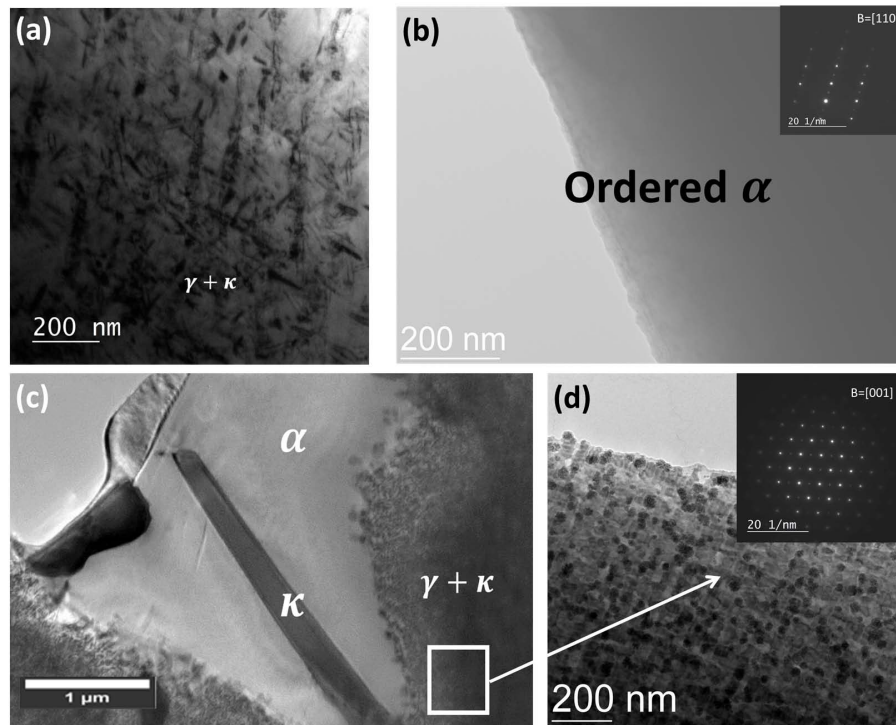
17

Figure 7: (a) TEM bright-field image of the γ phase of Fe-15Mn-10Al-0.8C-5Ni isothermally annealed at $500°C$ showing the formation of κ-carbides. (b) TEM bright-field image of ordered α (transformed into NiAl-type B2 stringer) and corresponding SADP (B=[110]). (c) TEM micrograph taken from α phase of Fe-15Mn-10Al-0.8C subjected to isothermal holding at $500°C$ showing the needle-like morphology of a κ particle in this phase. (d) TEM micrograph and corresponding SADP demonstrating the formation of nano-sized (<50 nm) κ-phase in the γ phase of Fe-15Mn-10Al-0.8C.

3.5. Heat treatment at 700 °C

The microstructures of S1 and S2 after isothermal holding at $700°C$ are shown in Fig.8. Similar to $500°C$ isothermal holding, the α phase of S1 was entirely transformed to B2 stringer and no κ-carbide was observed in this phase. However, a very dense population of the κ-phase were formed in the grain interior of γ. The closely packed κ-carbides in the γ phase had a size of $\leq$150 nm. B2-type particles were, again, observed both at the γ grain boundaries and in the γ grain interiors. No significant change in the size of B2 particles were observed as the isothermal temperature increased. For S2, κ-carbide lamellar was formed in α-phase while no intermetallics were found in either γ or α. The κ-phase formed in the α-phase of S2 after isothermal annealing at $700°C$ was coarser than that formed in S2 isothermally annealed at $500°C$.
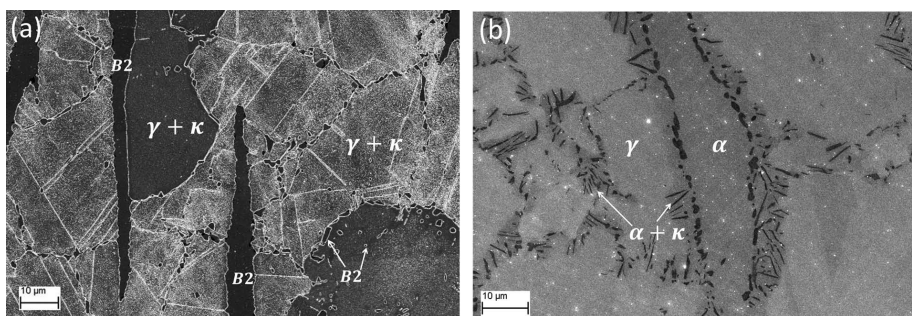
18

Figure 8: SEM micrographs (a) for Fe-15Mn-10Al-0.8C-5Ni after isothermal holding at $700°C$ showing the formation of κ-phase (after etching appeared as white) in γ phase while the α phase was transformed into B2-type intermetallics. In addition, the formation of B2 particles at grain boundaries and the γ grain interiors was observed and (b) for Fe-15Mn-10Al-0.8C after annealing at $700°C$ showing the formation of coarse boundary κ-carbides (darker phase).

₃₂₀ Fig.9 shows the simulations of multi-particle system in austenite (Fig.9a) and ferrite (Fig.9b). Table.1 shows a comparison between the simulated widths of κ-carbides in α for the isothermal holding temperature of $500°C$ and $700°C$ with those measured experimentally. During isothermal holding at $500°C$, a larger driving force for the κ-carbide precipitation exists. The difference in the evolution of κ-particles for different ₃₂₅ isothermal holding temperatures is due to the fact that during isothermal annealing at $500°C$ the γ decomposition kinetics into κ phase is retarded due to the lower diffusion rate of solutes, especially C, compared to the simulation carried at $700°C$. Thus, the κ-carbides formed at $500°C$ show a finer distribution compared to that formed at $700°C$. During the growth process, it is the diffusion of C during annealing treatment that ₃₃₀ primarily controls the morphology of κ particles [46, 61].

TEM-BF images of γ and α phases of S1 and S2 are shown in Fig.11. A more dense and closely packed population of cuboidal κ-carbides were observed in the γ phase of S1 compared to that formed after isothermal holding at $500°C$ (Fig.7a). Moreover, the average size of cuboidal κ-carbides after isothermal holding at $700°C$ increased to ₃₃₅ about 150 nm compared with those formed during the isothermal holding at $500°C$. For S2, the width of κ-particles increased with a higher annealing temperature: the average widths of the κ-particles at 500 and $700°C$ are 200 ± 27 nm and 500 ± 33 nm, respectively. These values are much greater than the widths of κ-particles reported in Ref. [47] where κ-particles with an average width 17 ± 7 at $500°C$ were observed.

This implies the great dependency of the morphology of the κ-particles on the composition. The coarser κ-particles formed in the current investigation in comparison to the previous studies [47] can be due to the higher amount of alloying elements (Al and Mn) available for the formation of this phase.
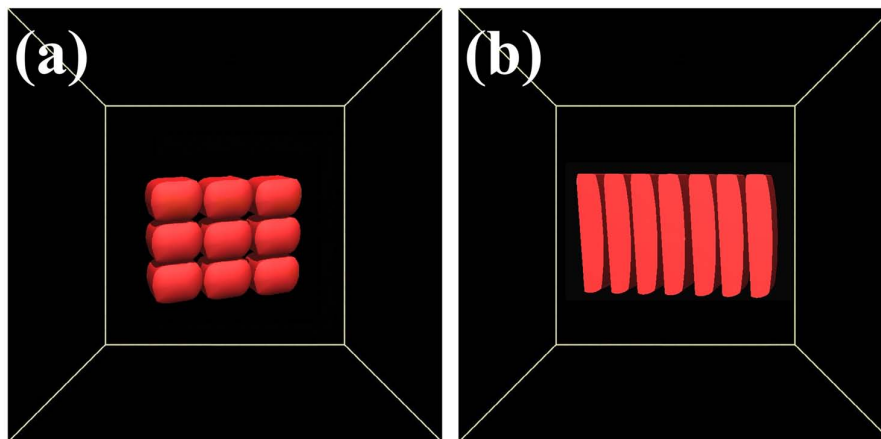

Figure 9: Multi particle phase-field simulations of κ-precipitates in (a) γ and (b) α for isothermal holding at $700^\circ C$ ($t^* = 60,000\Delta t$).

Table 1: Comparison between simulation results and experimental values.

Description	simulation		experiment	
	$500^\circ C$	$700^\circ C$	$500^\circ C$	$700^\circ C$
Isothermal temperature				
Width (nm)	188	519	200 ± 27	500 ± 33

Fig.10 shows the effect of partitioning of Mn on the morphology of a κ-particle. At initial stages of simulation where the Mn content of κ is almost twice that of α phase ($\frac{C_{Mn,\kappa}}{C_{Mn,\alpha}}$, blue curve), the minimum value of the energy/volume ratio occurs at an aspect ratio (length of the particle/width of the particle) equal to 6. At later stages when the ratio of the Mn contents becomes larger, the minimization of energy shifts towards higher aspect ratios. In other words, as Mn partitions into the κ-particle the morphology becomes rod-like. This happens because the partitioning of Mn into the particle increases the lattice misfit between κ and α (by increasing the lattice parameter of κ [68]) and thus, in order for elastic strain energy to become minimum, the particle morphology changes to rod (larger length/width ratio).
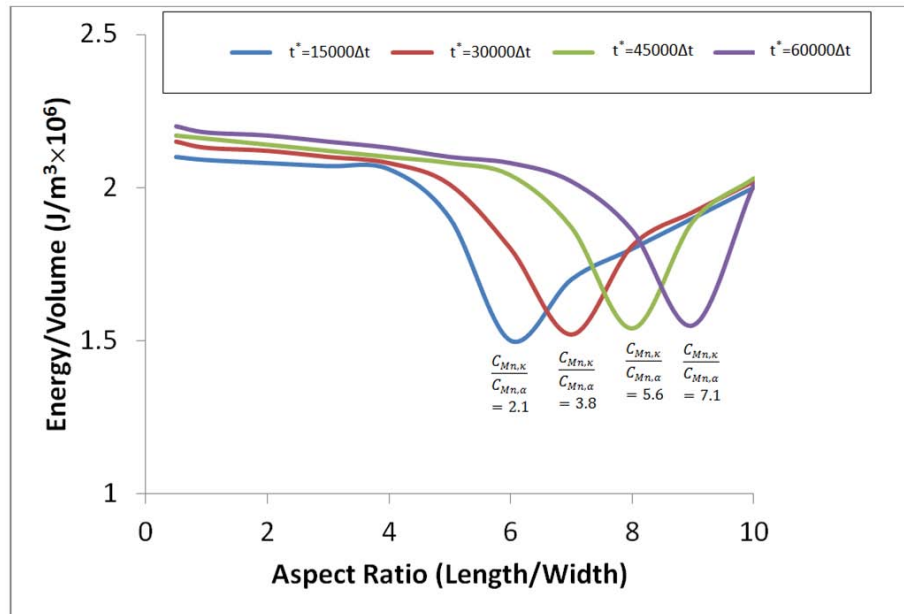
20

Figure 10: The ratio of energy/volume of a κ-particle as a function of time step and the elemental partitioning of Mn. The larger than unity the ratio, the severe the partitioning for the corresponding element.

The volume fraction of κ-particles in the α-phase increased by the increasing an-
355 nealing temperature from 7% to 14%, as can be seen by a comparison between Fig.11d

with Fig.7c. This can be due to the easier diffusion of constituent elements at a higher

annealing temperature. The growth mechanism of κ-carbide was reported [47] to be

nucleation-growth process, however, although it seemed to be the corresponding mech-

anism for κ formed in α, the formation of κ within the γ phase appeared to be due to
360 spinodal decomposition [78], as can is evident from the TEM micrographs taken from

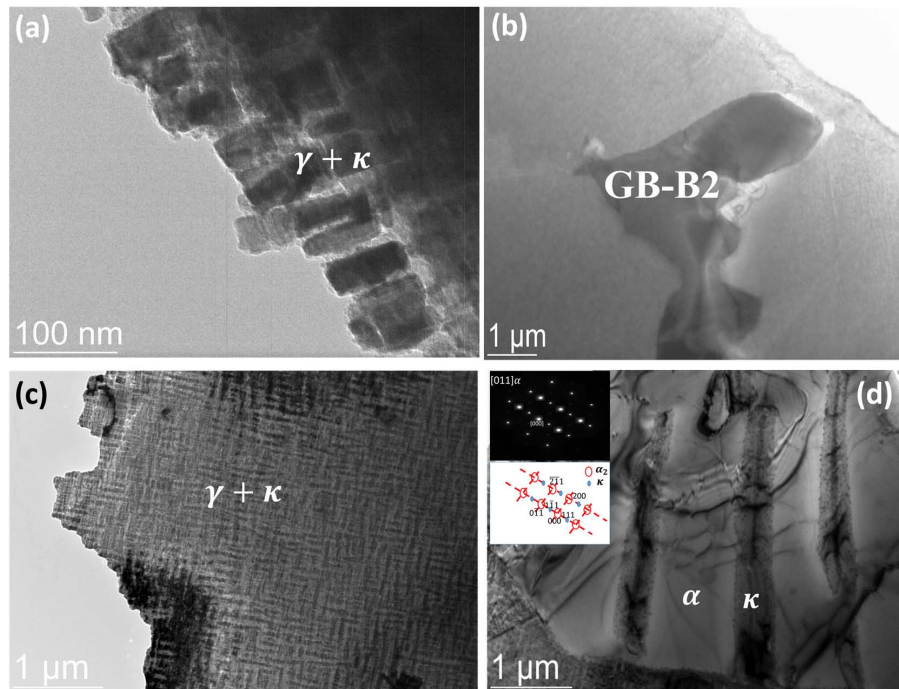the γ of both samples annealed at either 500 or $700^{\circ}C$.

21

Figure 11: (a) TEM bright-field image of the cuboidal κ-carbides formed within the γ matrix in Fe-15Mn-10Al-0.8C-5Ni after annealing at $700^\circ C$. (b) TEM bright field image of Fe-15Mn-10Al-0.8C-5Ni showing the formation of a coarse grain boundary B2 (GB-B2) at a triple point. (c) TEM bright-field micrograph of a γ grain in Fe-15Mn-10Al-0.8C after isothermal holding at $700^\circ C$, showing the densely populated cuboid κ-particles in this phase with a size of $< 50nm$. (d) TEM image of coarse needle-like κ-carbides in the α phase of Fe-15Mn-10Al-0.8C and the corresponding SADP.

Fig.12 shows the SEM micrograph and TEM bright field image of a depleted zone at γ-α boundary in S1 after isothermal annealing at $700^\circ C$. As can be seen in this figure, a coarse B2 intermetallic was formed at γ-α grain boundary. This prevented

365 the formation of κ-phase in the vicinity of the grain boundary, because Al was consumed by the NiAl-type B2 intermetallic compound formed at the boundary. Similar phenomenon was also observed for the same sample annealed at $500^\circ C$. In contrast, no depleted zone was found for S2 during isothermal holding at 500 nor at $700^\circ C$.

22
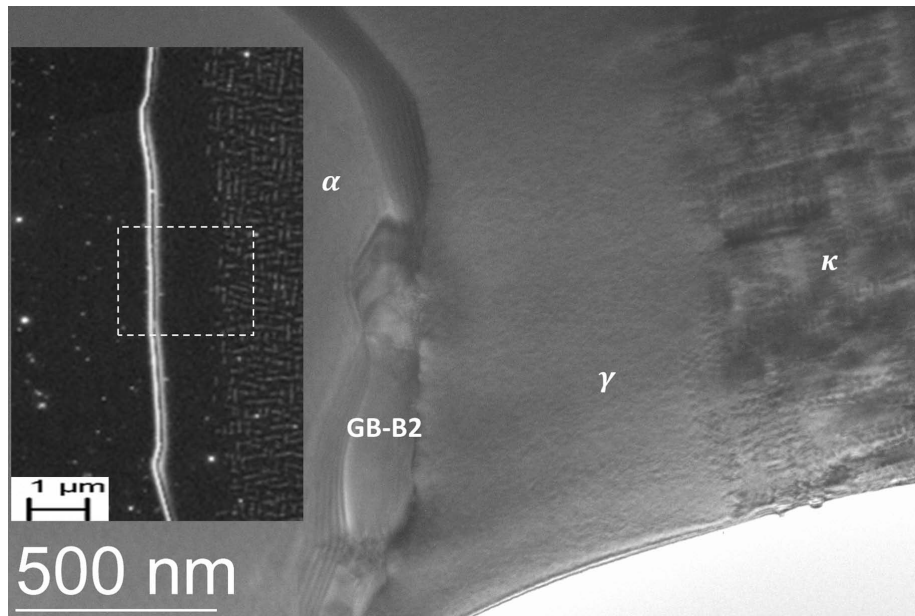
Figure 12: SEM and TEM bright-field images of a depleted zone in the neighbourhood of a coarse GB-B2 particle.

3.6. Heat treatment at 900 °C

₃₇₀ Fig.13 shows the microstructures of S1 (Fig.13a) and S2 (Fig.13b) after isothermal

holding at $900°C$. As is shown in Fig.13a, coarse, densely packed NiAl-type B2 inter-

metallics were formed in the γ grains. Almost all γ-γ grain boundaries were decorated

by B2 precipitates. The morphology of B2 particles were rod-type and triangle-type

with size of 2-7 μm. Similar phenomenon was observed for the S1 after annealing at

₃₇₅ $900°C$ (Fig.13b). However, B2 particles were of FeAl-type. B2 particles were also

formed at γ grain boundaries similar to what was observed for S1 after annealing at

this temperature. No κ was found in the microstructure of S2 nor in that of S1. The

absence of κ at $900°C$ was also supported by thermodynamic calculations [79].

Figure 13: (a)The microstructure of Fe-15Mn-10Al-0.8C-5Ni after annealing at $900^\circ C$ showing the formation of coarse closely packed B2 NiAl-type particles in $\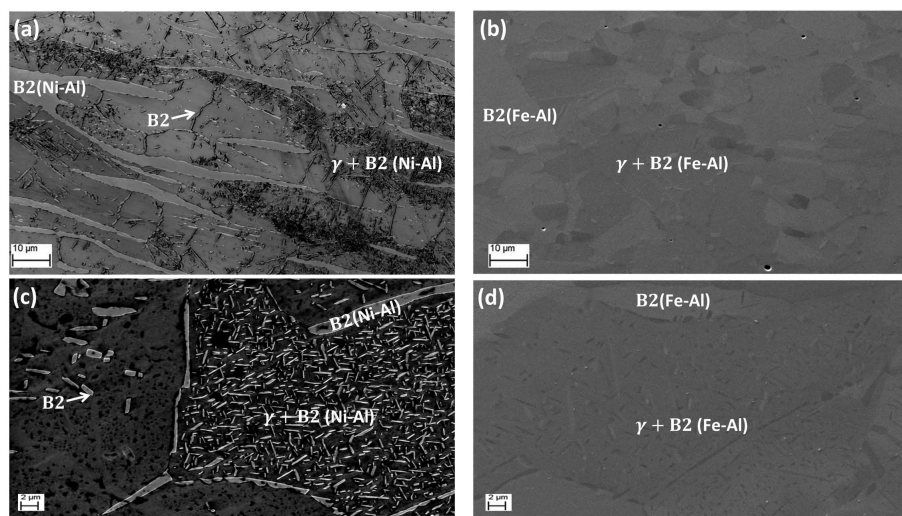gamma$. The coarse B2 precipitates were also formed at γ grain boundaries. (b) SEM micrograph taken from Fe-15Mn-10Al-0.8C after isothermal holding at $900^\circ C$ showing the formation of B2 FeAl-type intermetallics. The morphology and size of particles were similar to that observed for Fe-15Mn-10Al-0.8C-5Ni.

    A close inspection showed that in addition to coarse triangle-like B2 particles with

380 sharp edges (Fig.14b), nano-sized disk-like B2 precipitates were also formed in α. Similar morphologies of B2, namely triangle-like and disk-like, with equivalent sizes were detected in the microstructure of S2. Although coarse B2 particles were observed at lower isothermal holding temperatures, $500^\circ C$ and $700^\circ C$, the fine disk-like B2 particles were only observed after annealing at $900^\circ C$. As is evident in this figure, κ

385 was not formed at this temperature. Fig.14c shows the simulated front view of a disk-like FeAl-type B2 in α matrix. Fig.14d shows a NiAl-type B2 precipitate in γ matrix. The compositional variation of a B2 precipitate formed in S1 shows the similar trend as was predicted by our simulation (Fig.2b). The formation of disk-like B2 particles in α matrix corresponds to the second jump in the simulated COP for annealing at

390 $900^\circ C$ (Fig.1c). This means that during annealing at higher temperatures, Ni atoms partition and form disk-like B2 particles within the α matrix together with Al atoms. This means that Ni and Al are depleted within the α phase and thus this phase becomes softer compared to the situation where α phase completely transformed into B2 stringer bands. Hence, the microstructure has a desirable mixture of strength and ductility.
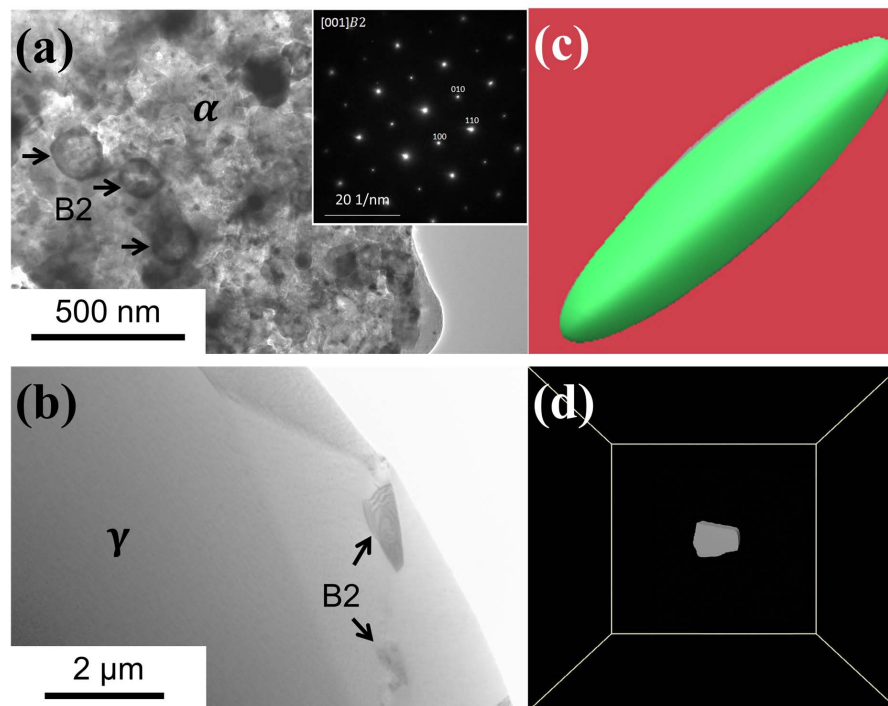
24

Figure 14: TEM micrograph taken from the BCC phase of Fe-15Mn-10Al-0.8C-5Ni showing nanosized disk-like B2 NiAl intermetallics with sizes of <150 nm and the corresponding SADP. Similar morphologies and sizes were observed for FeAl-type B2 particles in the BCC phase of Fe-15Mn-10Al-0.8C after annealing at $900°C$. (b) A coarse triangle-like FeAl-type B2 particle with a size of a few μm in a γ matrix for Fe-15Mn-10Al-0.8C after annealing at $900°C$. (c) Phase-field simulation of a FeAl-type B2 precipitate in the α matrix $t^* = 10000\Delta t$. (d) Simulated morphology of a NiAl-type B2 particle in the γ phase $t^* = 10000\Delta t$.

3.7. Heat treatment at $1050°C$

Fig.15 shows the microstructures of (a) S1 and (b) S2 after annealing at $1050°C$. A simple comparison between this figure and Fig.13 reveals that (i) the volume fraction of both coarse NiAl-type and FeAl-type B2 intermetallic compounds in the austenite phase of S1 and S2 decreased from 38% (isothermal holding at $900°C$) to 11% (isothermal holding at $1050°C$) and (ii) the microstructures of both S1 and S2 are much more uniform in terms of the distribution of B2 particles in the α phase after isothermal holding at $1050°C$ compared to that after annealing at $900°C$. This was due to the fact that during the annealing at $1050°C$ the driving force for the formation of B2 phase was much smaller (smaller undercooling ($\approx 1200°C - 1050°C$)) compared with that during the isothermal holding at $900°C$ ($\approx 1200°C - 900°C$). Fig.16 also demon-

25

strate that disk-like B2 particles were uniformly distributed in the ferrite phase of both S1 and S2. These observations meant that mechanical properties of samples could be improved after annealing at $1050°$.
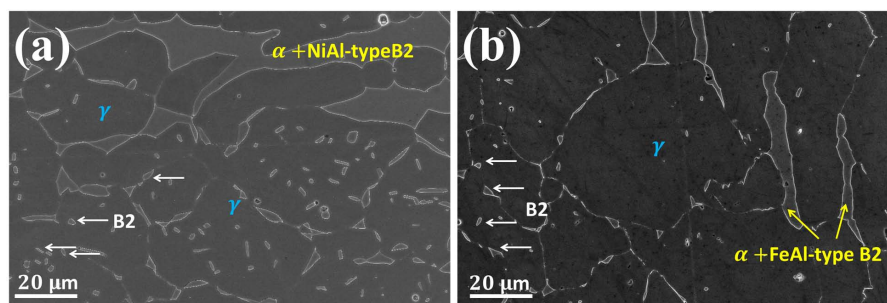
Figure 15: SEM micrographs of heat treated samples at $1050°C$ for (a) Fe-15Mn-10Al-0.8C-5Ni and (b) Fe-15Mn-10Al-0.8C. B2 particles in the γ matrix are shown with white arrows.
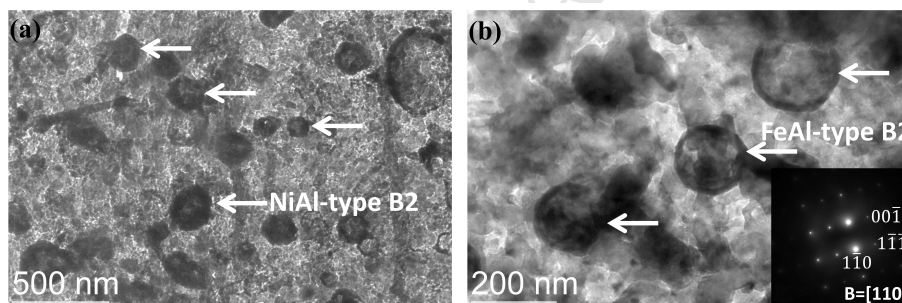
Figure 16: TEM bright-field image of (a) disk-like NiAl-type B2 particles formed in ferrite matrix of Fe-15Mn-10Al-0.8C-5Ni and (b) of disk-like FeAl-type B2 particles formed in the ferrite matrix of Fe-15Mn-10Al-0.8C and corresponding SADP. The images were taken from samples heat treated at $1050°C$.

3.8. The variation of chemical compositions of ordered phases

410   The post-annealing compositions of samples are summarized in Table. 2. Starting with S1, Mn, Al, and Ni contents of B2 phase (in both ordered α and in γ) increased with increasing annealing temperature because of an easier diffusion of substitutional atoms at higher temperatures. Al content of B2 stringer (initially α phase) was higher than those formed in γ whereas the Ni contents were almost the same. This means that

415   B2 stringer are much harder than B2 particles formed within the γ matrix [75]. Al and Ni contents of κ phase in γ remained almost constant whereas a significant increase in

26

the Mn content of κ-phase occurred as the annealing temperature increased. Similarly in S2, Al content of κ-carbides in both α and γ slightly increased whereas Mn content of the carbides increased considerably. In general, the Mn content of κ formed in the

420 γ matrix was higher than that of lamellar κ in the α phase. Here, we observed the formation of non-stoichiometric κ-carbides in both steels, in agreement with previous reports on κ-carbides existing over a range of varying Mn and Al contents [42, 78]. According to these results, Al is energetically stable inside either B2 intermetallic or κ and both product phases are competing sites for Al.

Table 2: Chemical compositions of κ-carbide and B2 compounds as a function of isothermal annealing temperature and the matrix within which they formed. Please note that the chemical compositions for B2 in the α phase for isothermal holdings at $500^\circ C$ and $700^\circ C$ refer to ordered α or namely stringer B2 bands.

Matrix			α				γ			
Temperature(°C)			500	700	900	1050	500	700	900	1050
Fe-15Mn-10Al-0.8C-5Ni	B2	Mn	3.1	3.2	3.3	3.2	4.4	4.5	4.5	4.5
		Al	18.1	19.5	20.4	21.3	14.5	15.6	17.1	18.7
		Ni	8.2	10.4	15.1	19.2	9.1	9.4	9.7	10.1
	κ-carbide	Mn	-	-	-	-	18.9	22.5	-	-
		Al	-	-	-	-	8.1	8.3	-	-
		Ni	-	-	-	-	0.1	0.1	-	-
Fe-15Mn-10Al-0.8C	B2	Mn	-	-	3.3	3.2	-	-	5.1	5.1
		Al	-	-	22.8	24.6	-	-	18.3	19.1
	κ-carbide	Mn	18.4	24.8	-	-	20.4	25.1	-	-
		Al	10.2	10.7	-	-	9.7	10.1	-	-

425 Despite the fact that κ-phase formed at $500^\circ C$ had a stronger undercooling and thus an increased driving force for pro-eutectoid ferritic transformation, the Mn content of κ-phase increased with increasing annealing temperature because of easier diffusion of relatively large substitutional Mn atoms at higher temperature. This in turn led to an increase in the contents of Mn in the γ phase and thus the formation of κ-carbide with

430 a higher content of Mn. This finding is in contradiction with the results reported in Ref.[47] where the authors explained the higher content of Mn in κ-carbides at lower annealing temperature ($500^\circ C$) in terms of stronger driving force for the formation of κ-phase at lower isothermal holding temperature.

The Ni content of B2 particles also increased with increasing annealing tempera-

435 ture. This can be also due to the easier diffusion of Ni atoms at higher temperatures ($900°C$ and $1050°C$). Breuer et al. conducted a series of experiment and measured the enthalpy of formation of $B2 - Fe_{1-x} - Al_x$ and $B2 - (Fe, Ni)_{1-x} - Al_x$ at 1073K. Their results showed that generally enthalpy of formation of $B2 - (Fe, Ni)_{1-x} - Al_x$ is of greater magnitude than that of $B2 - Fe_{1-x} - Al_x$. It was also shown that starting
440 with binary $B2 - Fe_{1-x} - Al_x$ and replacing Fe with Ni, $B2 - (Fe, Ni)_{1-x}Al_x$ while keeping the Al content at a constant value, the enthalpy of formation becomes increasingly more negative [75]. In other words, increasing the Ni content of B2 can result in the formation of a harder B2 phase. More information about composition change with increasing annealing temperature as well as EDX maps for each holding temperature
445 are presented in supplementary information.

3.9. Mechanical properties

To confirm our hypotheses about the effects of following microstructural changes on the mechanical properties:

(i) the formation of disk-like B2 particles after annealing at $900°C$ and $1050°C$

450 (ii) the increase in the Mn content of κ-carbides with increasing annealing temperature which can result in the formation of harder κ-carbides

(iii) the increase in the volume fraction of needle-like κ-carbides formed in the α phase of S2 after annealing at $700°C$ compared to that after isothermal holdeing at $500°C$

455 (iv) the formation of much more uniform microstructure and decreased in the volume fraction of B2 particles formed with the γ matrix of both S1 and S2 after isothermal holding at $1050°C$ compared to that formed at $900°C$

(v) the increase in the Ni and Al contents of B2 phase with increasing annealing temperature which may lead to formation of harder strengthening secondary phase
460 (B2)

We performed tensile testing of the samples annealed at these four temperatures. The mechanical response of the as-quenched state is shown in Fig. 17 by green colour:

ultimate tensile strength (UTS) of as-quenched S1 was measured to be 630 MPa with an elongation (E) of 22.4%; the UTS of as-quenched S2 was determined to be 590

465 MPa with an El of 25.7%. As shown in this figure, the subsequent annealing at $500°C$ significantly increased the UTS for both samples while reduced their ductility: UTS increased to 980 MPa and El decreased to 10% for S1; UTS increased to 840 MPa for S2 and its El reduced to 11%.

Fig.17 shows that by increasing the isothermal annealing temperature from $500°C$

470 to $1050°C$, the UTS increases significantly (from 980 MPa to 1350 MPa for S1 and from 840 MPa to 1040 MPa for S2) whereas the ductility remarkably improved the elongation of S1 to 22% and that of S2 to 25%. In general, S1 had higher UTS and lower elongation than S2. This is due to the formation of GB-B2 and B2 stringer phases in S1 which added extra strengths and reduced the ductility of the steel. Fig.17a,b show

475 that by increasing the isothermal annealing temperature from $500°C$ to $700°C$, the ultimate tensile strength (UTS) increased slightly: in S1 from 980 MPa to 1040 MPa and in S2 from 840 MPa to 910 MPa. For S1, the dense closely packed populations of κ-carbides formed after annealing at $700°C$ resulted in the enhancement of the strength compared to that of the sample annealed at $500°C$. Moreover, the increase in the

480 Mn content of κ phase makes this phase harder and thus increases the strength. For S2, in addition to the increased number of Mn-C bonds which results in harder κ-carbides [68], the increase in the volume fraction of needle-like κ-phase after annealing at $700°C$ led to an increase in the strength of the material. The formation of depleted zones in the microstructure of S1 has a negative effect on the mechanical properties and

485 the increment of strength. That explains why the value of UTS of S1 is only slightly higher than that of S2, despite the coexistence of both hard B2 intermetallic particles and κ-carbides in the microstructure of S1.

At $900°C$, κ-carbides were not form in the microstructures of S1 and S2. This explained the larger ductility of S2 isothermally hold at $900°C$ compared to that of the

490 same material annealed at $700°C$. However, S1 showed almost the same ductility after annealing at $900°C$ to that isothermally hold at $700°C$. This was due to the formation of hard, coarse and densely packed population of NiAl-type B2 particles within the γ phase interiors of S1. NiAl-type B2 particles are not shearable by gliding dislocation

29

whereas κ-carbide has a shearable nature [41, 83]. Moreover, the formation of coarse

495 GB-B2 also resulted in the reduction of the ductility of S1.

Comparing the samples annealed at $900°C$ and $1050°C$, the strength of both S1 and S2 slightly increased (<20 MPa) while the ductility significantly improved. This can be due to the formation of more uniform distribution of B2 particles as well as the reduction of the volume fraction of them in the γ phases of S1 and S2. The slight

500 increase in the strength of the materials can be explained by the increase of the Ni and Al contents of B2 particles in S1 and the Al content of B2 phase in S2 resulting in the formation of harder B2 particles. The strength of S1 after annealing at $900°C$ and $1050°C$ was about 300 MPa higher than that of S2 isothermally hold at the same temperature because Ni-Al bonds in the B2 phase are generally stronger than Fe-Al

505 bonds [75, 76]. This also explains the larger ductility of S2 in comparison with that of S1: B2 particles formed in the microstructure of S2 was not as strong as those formed in the microstructure of S1.

The fracture surfaces of both steels were examined under SEM as is shown in the Fig.17. The fracture mechanism for both S1 and S2 samples annealed at $500°C$ and

510 $700°C$ was mainly cleavage, and it became more fibrous for isothermal holding at $1050°C$, confirming their significantly improved ductility. In general S2 showed a larger ductility compared to S1 because after annealing at $500°C$ and $700°C$, the microstructure of S2 was devoid of B2 phase while significant amount of B2 particles were formed in the γ phase of S1. Moreover, the α phase of S1 transformed into B2

515 stringer bands resulting in additional strength and in the reduction of ductility.

In an elegant study, Gutierrez-Urrutia and Raabe [81] investigated the strain hardening and the evolution of dislocation configuration in lightweight Fe-Mn-Al-C steels. They showed that this type of steels exhibit a noticeable evolution of the dislocation substructure during deformation and attributed this to the effect of solute carbon on

520 dislocation movement. The results demonstrated that aluminium and carbon significantly increases the stacking fault energy (SFE). In addition carbon provides strong dislocation-solute interaction. They argued that high carbon content in solid solution retards the formation of dislocations associated with cross-slip and shifts them to high macroscopic stress levels. Welsch et al [82] also studied the strain hardening

30

⁵²⁵ of lightweight steels by dynamic slip band refinement. They showed that the presence of short range order (SRO) and finely distributed long range ordered (LRO) clusters remarkably increases the stress required to "bow out" single dislocations in comparison with disordered crystal. The abovementioned effects together with the formation of various ordered precipitates thus elucidate the observed mechanical properties of the

⁵³⁰ samples under study.
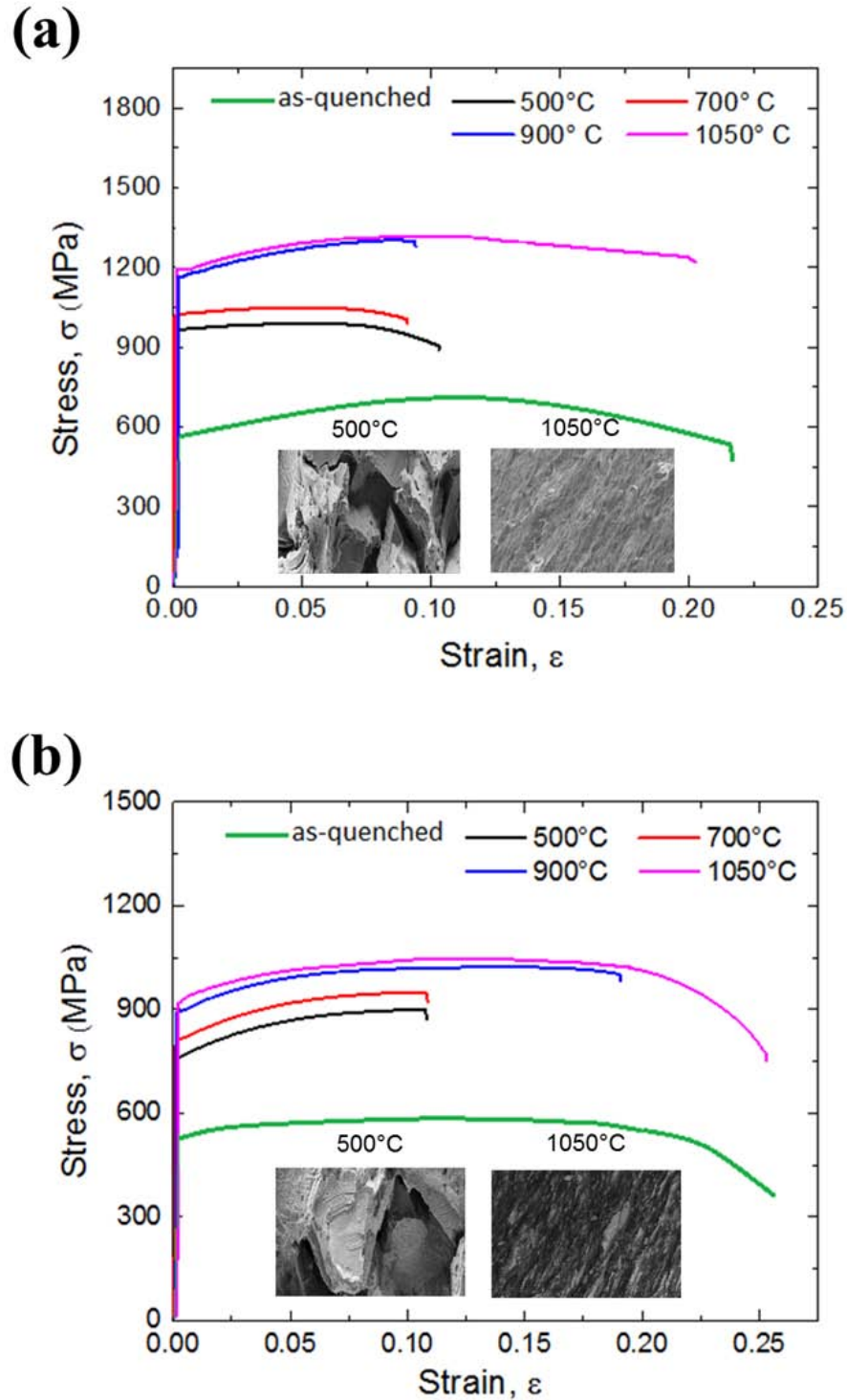
Figure 17: (a) Room-temperature tensile properties of Fe-15Mn-10Al-5Ni-0.8C (S1) after isothermal annealing at $500^{\circ}C$, $700^{\circ}C$, $900^{\circ}C$ and $1050^{\circ}C$. (b) Room-temperature tensile properties of Fe-15Mn-10Al-0.8C (S2) after isothermal annealing at $500^{\circ}C$, $700^{\circ}C$, $900^{\circ}C$ and $1050^{\circ}C$. Fracture surfaces for both samples at $500^{\circ}C$ and $1050^{\circ}C$ are also shown within the graphs.

4. Summary

In summary, we investigated the microstructural evolution of Fe-15Mn-10Al-0.8C-5Ni (S1) and Fe-15Mn-10Al-0.8C (S2) (all in wt.%) duplex steel through phase-field modelling and during the isothermal annealing at $500°C$, $700°C$, $900°C$, $1050°C$.
535 Fig.18 shows a schematic overview of the microstructural evolutions of S1 and S2. Table.3 summarizes the formed phases at each isothermal temperature and the corresponding mechanical properties. Various aspects of the formation of ordered phases discussed in this paper are listed below.

Table 3: Summary of microstructural modifications and the variations of mechanical properties as a result of different annealing temperatures.

| Alloy		500°C	700°C	900°C	1050°C
Fe-15Mn-10Al-0.8C-5Ni	Matrix phase	γ	γ	$\gamma + \alpha$	$\gamma + \alpha$
	Precipitations	Cuboidal κ (<100 nm) Coarse B2 particles (2-7 nm) B2 stringer bands	Cuboidal κ (<150 nm) Coarse B2 particles (2-7 nm) B2 stringer bands	Coarse B2 particles (2-7 nm) Disk-like B2 ($\approx$ 200 nm)	Coarse B2 particles (2-4 nm) Disk-like B2 ($\approx$ 200 nm)
	Mechanical properties	UTS: 960 MPa Elongation:10.2	UTS: 980 MPa Elongation:9.8	UTS: 1335 MPa Elongation:10.4	UTS: 1350 MPa Elongation:22
Fe-15Mn-10Al-0.8C	Matrix phase	$\gamma + \alpha$	$\gamma + \alpha$	$\gamma + \alpha$	$\gamma + \alpha$
	Precipitations	Cuboidal κ (<90 nm) Coarse B2 particles (2-4 nm) needle-like κ (width of 200 $\pm$ 33 nm)	Cuboidal κ (<90 nm) Coarse B2 particles (2-4 nm) needle-like κ (width of 500 $\pm$ 33 nm)	Coarse B2 particles (2-4 nm) Disk-like B2 ($\approx$ 200 nm)	Coarse B2 particles (2-4 nm) Disk-like B2 ($\approx$ 200 nm)
	Mechanical properties	UTS: 840 MPa Elongation:11.3	UTS: 910 MPa Elongation:11.3	UTS: 1015 MPa Elongation:18	UTS: 1040 MPa Elongation:25
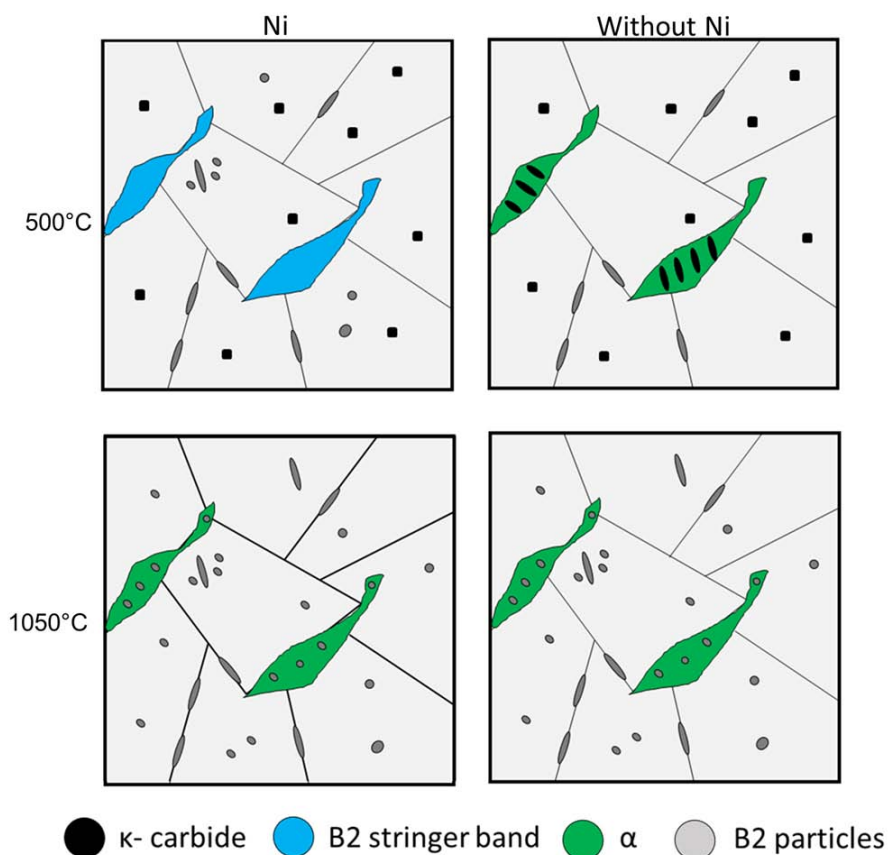
Figure 18: Schematic overview of the microstructural evolution of the materials under investigation as the annealing temperature increases.

1. Our simulations on B2 intermetallic compounds showed that the ordering in the
₅₄₀ BCC (α) occurs in two discrete stages: This first stage - shorter times and lower temperatures ($500^\circ C$ and $700^\circ C$) - corresponds to the ordering of disordered α, whereas the second stage is activated at higher temperatures ($900^\circ C$ and $1050^\circ C$) and correlates with the formation of disk-like B2 particles within the ordered α phase. The formation of Ni-enriched disk-like B2 particles in a triplex
₅₄₅ lightweight steel (γ, α and B2) can significantly improve the room-temperature tensile properties of the material by providing increased resistance to shear and favourable high ductility (disordered γ and α phases).

34

2. The simulations on κ-carbides clearly demonstrate that the morphological evolution of κ-carbide is highly dependent on the matrix within which it forms and on the energetic interactions between the interfacial and elastic strain energy.

3. Starting with S1, we observed:

(i) After annealing at $500°C$, the microstructure consisted of coarse B2 particles, frequently with sharp edges and flat interfaces, formed within the γ grains interiors and at the grain boundaries, and nanosized κ-carbides dispersed within the γ phase and B2 stringer bands.

(ii) After annealing at $700°C$, a dense closely packed population of κ-carbides were formed in the γ phase. Coarse B2 particles were also present both within the γ grains and at the grain boundaries. B2 stringer bands was also formed by the ordering process of α phase.

(iii) After annealing at $900°C$, a dense population of coarse B2 particles were formed in the γ phase while nanosized disk-like Ni-enriched B2 particles were formed in the α phase. Hence, the B2 stringer bands formed after annealing at $500°C$ and $700°C$ was transformed into α+disk-like B2 particles. No κ-carbides were found in the microstructure.

(iv) After annealing at $1050°C$, a more uniform distribution of B2 phase within γ was observed. The volume fraction of coarse B2 particles in the γ phase was reduced due to the reduction of undercooling and thus the decrease in the driving force for the formation of B2 phase. Nanosized disk-like B2 particles was also found within the α-phase.

With increasing annealing temperature, we observed an increase in (all in wt.%):

(i) the constituent elements of B2 particles formed in the γ phase of S1: Ni content increased from 9.1 to 10.1, Al content increased from 14.5 to 18.7 and Mn content remained almost constant.

(ii) the constituent elements of B2 stringer bands formed after annealing at $500°C$ and $700°C$: Ni content increased from 8.2 to 10.4, Al content increased from 18.1 to 19.5 whereas Mn content remained almost constant.

35

(iii) the constituent elements of nanosized disk-like B2 particles formed after annealing at $900°C$ and $1050°C$: Ni content increased from 15.1 to 19.2, Al content increased from 20.4 to 21.3 while Mn content did not change significantly.

(iv) the constituent elements of cuboidal κ-carbides formed within the γ phase of S1 after isothermal holdings at $500°C$ and $700°C$: Mn content increased from 18.9 to 22.5, Al content slightly increased from 8.1 to 8.3 while Ni content remained constant.

We performed tensile testing on S1 and it was found that:

(i) The samples annealed at $500°C$ and $700°C$ exhibited similar mechanical properties (UTS≈980 MPa and elongation around 10%). This was due to the formation similar microstructures in the samples after annealing at these isothermal holding temperature e.g. nanosized cuboidal κ-carbides and coarse B2 particles in γ, and B2 stringer bands formed by the ordering of the α phase. The fracture surfaces of the samples were mostly cleavage.

(ii) The samples annealed at $900°C$ and $1050°C$ showed almost the same strength (UTS= 1350 MPa). However, the sample annealed at $1050°C$ had a larger ductility (elongation around 22%) because of the less volume fraction of coarse B2 particles in the γ and their uniform distribution.

4. For S2, the following microstructural changes were observed:

(i) After annealing at $500°C$, the microstructure consisted of cuboidal κ-carbides in the γ and coarse needle-like κ carbides with a width of 200 nm $\pm$ 33 in the α. No B2 particles were found within the microstructure.

(ii) After annealing at $700°C$, cuboidal nanosized κ-carbides and coarse pearlitic-like $\alpha + \kappa$ structure was observed. The volume fraction and the average width of needle-like κ-carbides was increased to 500±33 compared to those of the same structure formed after annealing at $500°C$.

36

(iii) After annealing at $1050°C$, no κ-carbides was formed in γ nor in the α
    phase. Instead, coarse FeAl-type B2 particles were found with the γ phase
    while nanosized disk-like FeAl-type B2 particles were observed in the γ.

(iv) After annealing at $1050°C$, the volume fraction of coarse B2 particles de-
    creased compared to the sample annealed at $900°C$. The more uniform
    distribution of B2 particles within the γ was also observed. Nanosized Al-
    enriched disk-like B2 precipitates were formed in the α phase.

With increasing the isothermal holding temperature, we observed an increase in
(all in wt.%):

(i) the Al content of B2 particles formed in the both disordered γ (from 18.3
    to 19.1) and α (from 22.8 to 24.6) phases after annealing at $900°C$ and
    $1050°C$.

(ii) the Mn content (from 20.4 to 25.1 in γ and from 18.4 to 24.8 in α) and Al
    content (from 9.7 to 10.1 in γ and from 10.2 to 10.7 in α) of κ-carbides
    after annealing at $500°C$ and $700°C$.

We performed tensile testing on S1 and it was found that:

(i) The samples annealed at $500°C$ and $700°C$ showed almost similar me-
    chanical properties (UTS$\approx$ 840 MPa and elongation around 10%). This
    was due to the formation similar microstructures in the samples after an-
    nealing at these two isothermal holding temperatures e.g. nanozised cuboidal
    κ-carbides, and a lamellar structure of $\alpha+\kappa$.

(ii) The samples annealed at $900°C$ and $1050°C$ showed almost the same
    strength (UTS$\approx$ 1050 MPa). However, the sample annealed at $1050°C$
    had a larger ductility (elongation around 27%) because of the less volume
    fraction of coarse B2 particles in the γ and their uniform distribution.

5. Comparing the microstructural evolution, chemical composition change and the
   variation of mechanical properties of S1 and S2, we can conclude that:

37

(i) For annealing at $500°C$ and $700°C$, it was observed that the microstructure of S1 consisted of γ, κ and NiAl-type B2 intermetallic (formed within γ interior grains, at grain boundaries and in a form of stringer bands by the ordering of the α phase). The microstructure of S2 characterized to be $\gamma+$ lamellar structure of $\alpha+\kappa$. In the γ phase of S2, nano-size cuboidal κ-carbides were formed whereas in the α phase of S2, coarse lamellar structure consisting of $\alpha + \kappa$ was observed with a width between 200 nm to 500 nm depending on the annealing temperature. No intermetallics were observed within the grains or at grain boundaries in S2. The additive Ni content (S1) led to the ordering of α phase and its transformation to stringer B2 compounds and prevented the formation of lamellar structure of $\alpha+\kappa$. The addition of Ni also resulted in the formation of coarse grain boundary-B2 (GB-B2). The existence of GB-B2 resulted in the formation of depleted zones in S1. This was not observed in the microstructure of S2. This study confirmed that the additive Ni content did not make a significant change in terms of mechanical properties after these two annealing temperature (less than 100 MPa increase in the UTS) while its addition may results in the formation of brittle GB-B2 and B2 stringer bands and led to 2% decrease in the elongation of S1 compared to that of S2.

(ii) For annealing at $900°C$ and $1050°C$, the microstructures of both S1 and S2 consisted of $\gamma+$coarse B2 particles and $\alpha+$disk-like B2 precipitates. S1 exhibited higher strength and smaller ductility due to the fact that Ni-Al bonds are much stronger than Fe-Al bonds formed in B2 intermetallic compounds.

(iii) In both samples, isothermal holding at $1050°C$ yielded the highest strength and the largest ductility.

(iv) Mn content of B2 particles were almost similar for both samples, whereas Al content of B2 was higher for S1 due to the high stability of Ni-Al bonds.

(v) The Mn content of κ-carbides were higher in S2 while the Al content was almost the same for both samples.

38

5. Conclusion

We investigated the strengthening mechanisms in a Fe-15Mn-10Al-0.8C lightweight steel with and without 5 wt. % Ni addition. The simulations clearly demonstrate that the morphological evolution of κ-carbide is highly dependent on the matrix within which it forms and on the energetic interactions between the interfacial and elastic strain. Our simulation and experimental observations confirm that the ordering in the BCC (α) occurs in two discrete stages. The addition of Ni into the alloys led to the ordering of (α) phase and its transformation to stringer B2 compounds and prevented the formation of lamellar structure of $\alpha + \kappa$. The addition of Ni also resulted in the formation of coarse grain boundary-B2 (GB-B2) which led to the formation of depleted zones. Therefore, at after these two annealing (500 C and 700 C) temperature the mechanical property of alloy with Ni was not improved. However, annealing at 900 C and 1050 C alloy exhibited higher strength and smaller ductility due to the fact that Ni-Al bonds are much stronger than Fe-Al bonds formed in B2 intermetallic compounds.

Additional Information

Acknowledgements

References

[1] H. Springer, D. Raabe, Rapidly alloy prototype: Compositional and thermo-mechanical high throughput bulk combinatorial design of structural materials based on the example of 30-Mn-1.2C-xAl triplex steels, Acta Mater. 60 (2012) 4950-4959.

[2] A. Inoue, Y. Kojima, T. Minemura, T. Masumoto, Microstructure and mechanical properties of ductile Ni3AI-type compound in Fe-(Ni, Mn)-AI-C systems rapidly quenched from melts, Metall. Trans. A 12A (1981) 1245-1253.

690   [3] K. Gschneidner, Jr, A. russell, A. Pecharsky, J. Morris, Z. Zhang, T. Lograsso, D. Hsu, C.H. Chester lo, Y. Ye, A. Slager, D. Kesse. A family of ductile intermetallic compounds, Nat. Mater. 2 (2003) 587-591.

[4] N. S. Stoloff, C. T. Liu, S.C. Deevi, Emerging applications of intermetallics, In-termetallics 8 (2000) 1313-1320.

695   [5] H.K.D.H. Bhadeshia, Computational Design of Advanced Steels, Scr. Mater. 70 (2014) 12-17.

[6] S.S. Sohn, B.J. Lee, S. Lee, J.H. Kwak, Microstructural analysis of cracking phenomenon occurring during cold rolling of (0.1∼0.7)C-3Mn-5Al lightweight steels, Met. Mater. Int. 21 (2015) 43-53.

700   [7] S.J. Park, B. Hwang, K.H. Lee, T.H. Lee, D.W. Suh, H.N. Han, Microstructure and tensile behavior of duplex low-density steel containing 5 mass% aluminum Scr. Mater. 68 (2013) 365-369.

[8] R. Rana, C. Liu, R.K. Ray, Evolution of microstructure and mechanical prop-erties during thermomechanical processing of a low-density multiphase steel for 705   automotive application, Acta Mater. 75 (2014) 227-245.

[9] Y.U. Heo, Y.Y. Song, S.J. Park, H.K.D.H. Bhadeshia, D.W. Suh, Influence of silicon in low density Fe-C-Mn-Al Steel, Metall. Mater. Trans. A 43 (6) (2012) 1731-1735.

[10] R.A. Howell, T. Weerasooriya, and D.C. Van Aken, Tensile, High Strain Rate 710   Compression and Microstructural Evaluation of Lightweight Age Hardenable Cast Fe-3Mn-9Al-XSi-0.9C-0.5Mo Steel, Int. J. Metalcasting 4, (2010) 7-18.

[11] K. Lee, S. -J. Park, J. Moon, J. -Y. Kang, T. -H. Lee, H. N. Han, β-Mn formation and aging effect on the fracture behaviour of high-Mn low-density steels, Scr. Mater. 124 (2016) 193-197.

[12] S.C. Tjong, Electron microscope observations of phase decompositions in an austenitic Fe-8.7 Al-29.7 Mn-1.04 C alloy, Mater. Charact. 24 (1990) 275-292.

[13] C.Y. Chao, C.H. Liu, Effects of Mn contents on the microstructure and mechanical properties of the Fe-10Al-xMn-1.0C alloy, Mater. Trans. 43 (2002) 2635-2642.

[14] W.K. Choo, K.H. Han, Phase constitution and lattice parameter relationships in rapidly solidified $((Fe_{0.65}Mn_{0.35})_{0.83}Al_{0.17-x}C)$ and $Fe_3Al_{-x}C$ pseudo-binary alloys, Metall. Trans. A 16 (1985) 5-10.

[15] K. Sato, K. Tagawa, Y. Inoue, Modulated structure and magnetic properties of age-hardenable Fe-Mn-Al-C alloys, Metall. Trans. A 21 (1990) 5-11.

[16] C.C. Wu, J.S. Chou, T.F. Liu, Phase Transformation in an Fe-10.1Al-28.6Mn-0.46C alloy, Metall. Mater. Trans. A 22 (1991) 2265-2276.

[17] X.F. Zhang, H. Yang, D.P. Leng, L. Zhang, Z.Y. Huang, G. Chen, Tensile deformation behaviour of Fe-Mn-Al-C low density steels, J. Iron and Steel Res. Int. 23 (2016) 963-972.

[18] M.C. Ha, J. Koo, J. Lee, S.W. Hwang, K. Park, Tensile deformation of a low density Fe-27Mn-12Al-0.8C duplex steel in association with ordered phases at ambient temperature, Mater. Sci. Eng. A 586 (2013) 276-283.

[19] G. Frommeyer, E. G. Drewes, B. Engl. Physical and mechanical properties of iron-aluminium-(Mn, Si) lightweight steels. Rev. de Métal. 97 (2000) 1245-1253.

[20] J. Herrmann, G. Inden, G. Sauthoff, Deformation behaviour of iron-rich iron-aluminium alloys at low temperatures. Acta Mater. 51 (2003) 2847-2857.

[21] D. Raabe, H. Springer, I. Gutierrez-Urrutia, F. Roters, M. Bausch, J.-B, Seol, M. Koyama, P.-P, Choi, K. Tsuzaki, Alloy Design, Combinatorial Synthesis, and Microstructure-Property Relations for Low-Density Fe-Mn-Al-C Austenitic Steels, JOM 66 (9) (2014) 1845-1856.

[22] D. Raabe, C. C. Tasan, H. Springer, M. Bausch, From high-entropy alloys to high-entropy steels, Steel Res. Int. 86 (10) (2015) 1127-1138.

[23] A. Zargaran, H. S. Kim, J. H. Kwak, N. J. Kim, Effects of Nb and C additions on the microstructure and tensile properties of lightweight ferritic Fe-8Al-5Mn alloy. Scr. Mater. 89 (2014) 37-40.

[24] I. Gutierrez-Urrutia, D. Raabe, High strength and ductile low density austenitic FeMnAlC steels: Simplex and alloys strengthened by nanoscale ordered carbides. Mater. Sci. Tech. 30 (2014) 1099-1104.

[25] I. Gutierrez-Urrutia, D. Raabe, Influence of Al content and precipitation state on the mechanical behavior of austenitic high-Mn low-density steels. Scr. Mater. 68 (2013) 343-347.

[26] H. Kim, D. W. Suh, N. J. Kim, Fe-Al-Mn-C lightweight structural alloys: a review on the microstructures and mechanical properties. Sci. Technol. Adv. Mater. 14 (2013) 014205.

[27] R. Oshima, C. Wayman, Fine structure in quenched Fe-Al-C steels, Metall. Trans. 3 (1972) 2163-2169.

[28] D. W. Suh, N. J. Kim, Low-density steels. Scr. Mater. 68 (2013) 337-338.

[29] W. J. Lu, R. S. Qin, Influence of κ-carbide interface structure on the formability of lightweight steels, Mater. Des. 104 (2016) 211-216.

[30] M. J. Yao, P. Dey, J. -B. Seol, P. Choi, M. Herbig, R. K. W. Marceau, T. Hickel, J. Neugebauer, D. Raabe, Combined atom probe tomography and density functional theory investigation of the Al off-stoichiometry of κ-carbides in an austenite Fe-Mn-Al-C low density steel, Acta Mater. 106 (2016) 229-238.

[31] C. Zhao, L. Zhang, F. Yang, T. Kang, Effect of annealing temperature on the microstructure and tensile properties of Fe-10Mn-10Al-0.7C low-density steel, Mater.Des. 91 (2016) 348-360.

42

[32] L. Zhang, R. Song, C. Zhao, F. Yang, Y. Xu, S. Peng, Evolution of the microstructure and mechanical properties of an austenite-ferrite Fe-Mn-Al-C steel, Mater. Sci. Eng. A 643 (2015) 183-193.

770 [33] L. Zhang, R. Song, C. Zhao, F. Yang, Work hardening behavior involving the substructural evolution of an austenite-ferrite Fe-Mn-Al-C steel, Mater. Sci. Eng. A 640 (2015) 225-234.

[34] F. Yang, R. Song, Y. Li, T. Sun, K. Wang, Tensile deformation of low density duplex Fe-Mn-Al-C steel, Mater. Des. 76 (2015) 32-39.

775 [35] K. T. Park, S. W. Hwang, C. Y. Son, J. K. Lee, Effects of Heat Treatment on Microstructure and Tensile Properties of a Fe-27Mn-12Al-0.8C Low-Density Steel, JOM 66 (2014) 1828-1838.

[36] I. Zuazo, B. Hallstedt, B. Lindahl, M. Selleby, M. Soler, A. Etienne, A. Perlade, D. Hasenpouth, V. Massardier-Jourdan, S. Cazottes, X. Kleber, Low-Density Steels: Complex Metallurgy for Automotive Applications, JOM 66 (2014) 1747-1758.

780

[37] R. Rana, Low-Density Steels, JOM 66 (2014) 1730-1733.

[38] H. Ding, D. Han, Z. Cai, Z. Wu, Microstructures and mechanical behavior of Fe-18Mn-10Al-(0.8-1.2)C steels, JOM 66 (2014) 1821-1827.

785 [39] Z.Q. Wu, H. Ding, H.Y. Li, M.L. Huang, F.R. Cao, Microstructural evolution and strain hardening behavior during plastic deformation of Fe-12Mn-8Al-0.8C steel, Mater. Sci. Eng. A 584 (2013) 150-155.

[40] I. Chumak, K. W. Richter, H. Ipser, Isothermal sections in the (Fe, Ni)-rich part of the Fe-Ni-Al phase diagram, J. Phase Equil. Diffus. 29 (2008) 300-304.

790 [41] S. H. Kim, H. Kim, N. J. Kim, Brittle intermetallic compound makes ultrastrong low-density steel with large ductility. Nat. 518 (2015) 77-79.

[42] G. Frommeyer, U. Brux, Microstructures and mechanical properties of high strength Fe-Mn-Al-C light-weight TRIPLEX steels, Steel Res. Int. 77 (2006) 627-33.

[43] I. S. Edwin, A. Bhowmik, R. S. Qin, Accelerated spheroidization Induced by high Intensity electric pulse in a severely deformed eutectoid steel. J. Mater. Res. 25 (2010) 1020-1024.

[44] Z. B. Jiao, J. H. Luan, M. K. Miller, C. T. Liu, Precipitation mechanism and mechanical properties of an ultra-high strength steel hardened by nanoscale NiAl and Cu particles. Acta Mater. 97 (2015) 58-67.

[45] Y. Z. Ji, A. Issa, T. W. Heo, J. E. Saal, C. Wolverton, L. Q. Chen, Predicting β' precipitate morphology and evolution in Mg-RE alloys using a combination of first-principles calculations and phase-field modeling, Acta Mater. 76 (2014) 259-271.

[46] J.B. Seol, D. Raabe, P. Choi, Y.R. Lim, C.G. Park, Atomic scale effects of alloying, partitioning, solute drag and austempering on the mechanical properties of high-carbon bainitic-austenitic TRIP steels, Acta Mater. 60 (2012) 6183-6199.

[47] J.B. Seol, D. Raabe, P. Choi, Y.R. Lim, C.G. Park, J.H. Park, C. G. Park, Direct evidence for the formation of ordered carbides in a ferrite-based low-density Fe-Mn-Al-C alloy studied by transmission electron microscopy and atom probe tomography, Scr. Mater. 68 (2013) 348-353.

[48] R. Chen, Q. Xu, B. Liu, Cellular automaton simulation of three-dimensional dendrite growth in Al-7Si-Mg ternary aluminium alloys, Comput. Mater.Sci. 105 (2015) 90-100.

[49] A. Rahnama, R. S. Qin, Modelling the microstructure of martensitic steels, Comput. Mater.Sci. 96 (2015) 102-107.

[50] A. Rahnama, R. S. Qin, Modelling the microstructure of polycrystalline austenite-martensite steels, Proc. ICME, John Wiley & Sons, Inc. (2015) 147-154.

44

[51] C. L. Lin, C. G. Chao, J. Y. Juang, J. M. Yang, T. F. Liu, Deformation mechanisms in ultrahigh-strength and high-ductility nanostructured FeMnAlC alloy, J. Alloys Compd. 586 (2014) 616-20.

[52] T. Xu, S. Sarkar, Y. Wang, Quantifying microstructures in isotropic grain growth from phase field modeling: Methods, Acta Mater. 60 (2012) 4787-99.

[53] M. Jamshidian, G. Zi, T. Rabczuk, Phase field modeling of ideal grain growth in a distorted microstructure, Comput. Mater. Sci. 95 (2014) 663-71.

[54] M. Militzer, Phase field modeling of microstructure evolution in steels, Curr. Opin. Solid State Mater. Sci. 15 (2011) 106-15.

[55] Y. Lu, L. Zhang, Y. Chen, Z. Chen, Y. Wang, Phase-field study for the pre-precipitation process of $L1_2$-Ni3Al phase in Ni-Al-V alloy, Intermetallics 38 (2013) 144-9.

[56] U. Grafe, B. Bottger, J. Tiaden, S. g. Fries, Coupling of multicomponent thermo-dynamic databases to a phase field model: application to solidification and solid state transformations of superalloys, Scr. Mater. 42 (2000)1179-1186.

[57] J. -L. Fattebert, M. E. Wickett, P. E. A. Turchi, Phase-field modeling of coring during solidification of AuNi alloy using quaternions and CALPHAD input, Acta Mater. 62 (2014) 89-104.

[58] A. G. Khachaturyan, Theory of Structural Transformation in Solids, Wiley, New York, 2008. 129.

[59] Y. Wang, D. Banerjee, C. C. Su, A. G. Khachaturyan, Field kinetic model and computer simulation of precipitation of $L1_2$ ordered intermetallics from F.C.C solid solution, Acta Mater. 46 (1998) 2983-3001.

[60] R. Poduri, L. Q. Chen, Computer simulation of morphological evolution and coarsening kinetics of δ' (Al_3Li) precipitates in Al-Li alloys, Acta Mater. 46(11) (1998) 3915-3924.

[61] A. Rahnama, R. Dashwood, S. Sridhar, A phase-field method coupled with CAL-PHAD for the simulation of $L'1_2$ ordered κ-carbide precipitates in both disordered γ and α phases in duplex low density steel, Comput. Mater. Sci. 126 (2017) 152-159.

[62] K. G. Chin, H. J. Lee, J. H. Kwak, J. Y. Kang, B. J. Lee, Thermodynamic calculation on the stability of $(Fe, Mn)_3AlC$ carbide in high aluminium steels, J. Alloys Compd. 505 (2010) 217-223.

[63] R. Poduri, L.Q. Chen, Computer simulation of atomic ordering and compositional clustering in the pseudobinary Ni3Al-Ni3V system, Acta Mater. 46 (1998) 1719-1729.

[64] D. Raabe, Computational Materials Science: The Simulation of Materials, Microstructures and Properties, Wiley, New York, 1998. 241.

[65] D. Liu, L. Zhang, Y. Du, J. Zhanpeng, Simulation of atomic mobilities, diffusion coefficients and diffusion paths in bcc_A2 and bcc_B2 phases of the Al-Ni-Fe system, J. All. Compd. 634 (2015) 148-155.

[66] T. Kitashima, H. Harada. A new phase-field method for simulating γ' precipitation in multicomponent nickel-base superalloys, Acta Mater 57 (2008) 2020-2028.

[67] R. S. Qin, H. k. D. J. Bhadeshia, Phase-field study of the effect of interface anisotropy on the crystal morphological evolution of cubic metals, Acta Mater. 57 (2009) 2210-2216.

[68] J.Y. Noh, H. Kim, Density functional theory calculations on κ-carbides, $(\mathrm{Fe}, \mathrm{Mn})_3\mathrm{AlC}$, J. Kor, Phys. Soc. 58 (2011) 285.

[69] T. Helander, J. Ågren, Diffusion in the B2-b.c.c. phase of the Al-Fe-Ni system-application of a phenomenological model, Acta Mater. 47 (1999) 1141-1152.

[70] Y. Liu, L. Zhang, Y. Du, D. Yu, D. Liang, Atomic mobilities, uphill diffusion and proeutectic ferrite growth in Fe-Mn-C alloys, CALPHAD 33 (2009) 614-423.

[71] M. Doi, Elasticity effects on the microstructure of alloys containing coherent precipitates, Prog. Mater. Sci. 40 (1996) 79-180.

[72] L. Q. Chen, J. Shen, Applications of semi-implicit Fourier-spectral method to phase field equations, Comput. Phys. Commun. 108 (1998) 147-158.

[73] C. H. Tsau, The effects of interfaces on the mechanical properties of Ni-Al-Fe intermetallics. Mater. Chem. Phys. 75 (2002) 296-300.

[74] J. w. Park, Anomalous yield behavior of hypo- and hyper-stoichiometric Fe_3Al intermetallic compounds, Intermetallics 10 (2002) 683.

[75] J. Breuer, A. Grun, F. Sommer, E. J. Mittemeijer, Enthalpy of formation of B2-$Fe_{1-x}Al_x$ and B2-$(Ni, Fe)_{1-x}Al_x$, Metall. Mater. Trans. B 32B (2011) 913-918.

[76] A. Rahnama, S. Spooner, S. Sridhar, Control of intermetallic nano-particles through annealing in duplex low density steel, Mat. Let. 189 (2017) 13-16.

[77] K.H. Han, J.C. Yoon, W.K. Choo, TEM evidence of modulated structure in Fe-Mn-Al-C austenitic alloys, Scr. Metall. Mater. 20 (1986) 33-36.

[78] W.K. Choo, J.H. Kim, J.C. Yoon, Microstructural change in austenitic Fe-30.0 wt % Mn-7.8 wt% Al-1.3 wt% C initiated by spinodal decomposition and its influence on mechanical properties, Acta Mater. 45 (1997) 4877-4885.

[79] K.G. Chin, H.J. Lee, J.H. Kwak, J.Y. Kang, B.J. Lee, Thermodynamic calculation on the stability of $(Fe,Mn)_3AlC$ carbide in high aluminium steels, J. Alloys Compd. 505 (2010) 217-223.

[80] E. Clementi, D. L. Raimondi and W. P. Reinhardt, Atomic Screening Constants from SCF Functions, J. Chem. Phys. 38 (1963) 2686.

[81] I. Gutierrez-Urrutia, D. Raabe, Multistage strain hardening through dislocation substructure and twinning in a high strength and ductile weight-reduced Fe-Mn-Al-C steel, Acta Mater. 60 (2012) 5791-5802.

[82] E. Welsch, D. Ponge, S.M. Hafez Haghighat, S. Sandlöbes, P. Choi, M. Herbig, S. Zaefferer, D. Raabe, Strain hardening by dynamic slip band refinement in a high-Mn lightweight steel, Acta Mater. 116 (2016) 188-199.

[83] W. Sanders, G. Sauthoff, Deformation behaviour of perovskite-type phases in the system Fe-Ni-Al-C. I: Strength and ductility of Ni_3AlC_x and Fe_3AlC_x alloys with various microstructures, Intermetallics 5 (1997) 361-375.